

Study on the Electronic Structure and Enhanced Photoelectrocatalytic Performance of $\text{Ru}_x\text{Zn}_{1-x}\text{O}/\text{Ti}$ Electrodes

Yanqun Shao (✉ yqshao1989@163.com)

Fuzhou University

Keke Feng

Fuzhou University

Jie Guo

Fuzhou University

Rongrong Zhang

Fuzhou University

Sijiang He

Fuzhou University

Xinli Wei

Fuzhou University

Yuting Lin

Fuzhou University

Zhanghao Ye

Fuzhou University

Kongfa Chen

Fuzhou University

Research Article

Keywords: $\text{Ru}_x\text{Zn}_{1-x}\text{O}/\text{Ti}$ electrode. first-principles calculation, electric collector, photoelectric synergistic catalysis

Posted Date: January 18th, 2021

DOI: <https://doi.org/10.21203/rs.3.rs-142224/v1>

License:   This work is licensed under a Creative Commons Attribution 4.0 International License.

[Read Full License](#)

Cover letter

Dear Longtu LI

We would like to submit the enclosed manuscript entitled “**Study on the electronic structure and enhanced photoelectrocatalytic performance of $\text{Ru}_x\text{Zn}_{1-x}\text{O}/\text{Ti}$ electrodes**” by Yanqun Shao, Keke Feng, Jie Guo, Rongrong Zhang, Sijiang He, Xinli Wei, Yuting Lin, Zhanghao Ye, Kongfa Chen, which we wish to public in the “Journal of Advanced Ceramics”.

As reported in our paper, $\text{Ru}_x\text{Zn}_{1-x}\text{O}/\text{Ti}$ electrodes with high photoelectrocatalytic (PEC) property were prepared by thermal decomposition method, and the first-principles calculation was adopted to analyze the effect of Ru content on the electronic structure of $\text{Ru}_x\text{Zn}_{1-x}\text{O}$ coatings. The results indicated that when Zn^{2+} replaced by Ru^{4+} in the lattice of ZnO, impurity energy level gradually appeared in ZnO band gap, which increased the number of photogenerated carriers. Besides, RuO_2 nanoparticles covered on ZnO nanorods surface, acting as highly efficient electron transfer channels and electrocatalytic active sites, could separate photogenerated electron-hole pairs and enhance PEC performance effectively. Meanwhile, adding Ru ions could offset such disadvantages of ZnO as oversized band gap and high recombination rate of photo-generated carrier. In this study, electrodes with an Ru content of 9.375mol% exhibited highest PEC efficiency, which could degrade organic substances dissolved in aqueous solution effectively (RhB 97%, 120min). and much higher than the combination of simple electrocatalysis (EC 12%) and photocatalysis (PC 50%), confirming the synergy of photoelectrocatalysis. Furthermore, the PEC degradation mechanism of the $\text{Ru}_x\text{Zn}_{1-x}\text{O}/\text{Ti}$ electrodes was also tentatively presented.

we believe that this paper will be attractive to the readers of Journal of Advanced Ceramics as the $\text{Ru}_{0.09375}\text{Zn}_{0.90625}\text{O}/\text{Ti}$ electrodes prepared in this study could degrade organic matter in industrial wastewater effectively, the effect of adding Ru ions on the electronic structure and PEC properties of ZnO was also analyzed and explained in detail, which provides a useful reference for further related research.

This paper has not been submitted to other institutions for publication, in whole or in part, and all the authors listed have approved that the manuscript is enclosed.

We have read and abided by the statement of ethical standards for manuscripts submitted to Journal of Advanced Ceramics.

Thank you so much for reading and reviewing our manuscript. looking forward to hearing from you soon.

Correspondence and phone calls about the paper should be directed to Yanqun Shao at the following address, phone and fax number, and e-mail address:

Corresponding author: Yanqun Shao (Professor)

Institute: College of Materials Science and Engineering, Fuzhou University

Address: College of Materials Science and Engineering, Fuzhou University, Xueyuan Road 2, Fuzhou, Fujian 350108, China.

Tel: +86-18950477698 Fax: +86-591-22866539

E-mail: yqshao1989@163.com

Referees

Yaobo Hu,

College of Materials Science and Engineering, Chongqing University, Chongqing 400045,
China

Tel: +86-13436117593

Email: yaobohu@163.com

He is an expert on this topic.

Yan Lei,

Department of Materials Engineering, College of Power and Mechanical Engineering, Wuhan
University, Wuhan, Hubei 430072 China

Tel: +86-18607131630

Email: yappee@126.com

She did this very well in the related field.

Yong Zheng,

College of Materials Science and Engineering, Nanjing University of Aeronautics and
Astronautics, Najing, Jiangsu 210026, China.

Tel: +86-13913017769

Email: zheng_only@263.net

He may be proficient in the content that I have written.

Study on the electronic structure and enhanced photoelectrocatalytic performance of $\text{Ru}_x\text{Zn}_{1-x}\text{O}/\text{Ti}$ electrodes

Yanqun Shao,^{a,b,*} Keke Feng,^a Jie Guo,^a Rongrong Zhang,^a Sijiang He,^a Xinli Wei,^a Yuting Lin,^a Zhanghao Ye,^a Kongfa Chen,^a

^a College of Materials Science and Engineering, Fuzhou University, Fuzhou, Fujian 350108, China

^b College of Zhicheng, Fuzhou University, Fuzhou, Fujian 350002, China

* Corresponding authors. Tel.: +86 18950477698

E-mail address: yqshao1989@163.com (Y. Shao)

All author. E-mail addresses: yqshao1989@163.com (Y. Shao)

1562569032@qq.com (K. Feng)

1340583406@qq.com (J. Guo)

1197853866@qq.com (R. Zhang)

1059720593@qq.com (S. He)

1091427214@qq.com (X. Wei)

331513557@qq.com (Y. Lin)

578169849@qq.com (Z. Ye)

kongfa.chen@fzu.edu.cn (K. Chen)

Abstract: Modification is one of the most important and effective methods to improve the photoelectrocatalytic (PEC) performance of ZnO. In this paper, the $\text{Ru}_x\text{Zn}_{1-x}\text{O}/\text{Ti}$ electrodes were prepared by thermal decomposition method and the effect of Ru content on those electrodes' electronic structure was analyzed through the first-principles calculation. Various tests were also performed to observe the microstructures and PEC performance. The results showed that as the Ru^{4+} transferred into ZnO lattice and replaced a number of Zn^{2+} , the conduction band of ZnO moved downward and the valence band went upward. The number of photogenerated electron-hole pairs increased as the impurity levels appeared in the band gap. In addition, ZnO nanorods exhibited a smaller grain size and a rougher surface under the effect of Ru. Meanwhile, the RuO_2 nanoparticles on the surface of ZnO nanorods acted as the electron-transfer channel, helping electrons transfer to the counter electrode and delaying the recombination of the electron-hole pairs. Specifically, the $\text{Ru}_x\text{Zn}_{1-x}\text{O}/\text{Ti}$ electrodes with 9.375mol% Ru exhibited the best PEC performance with a rhodamine B (RhB) removal rate of 97%, much higher than the combination of simple electrocatalysis (EC 12%) and photocatalysis (PC 50%), confirming the synergy of photoelectrocatalysis.

Keywords: $\text{Ru}_x\text{Zn}_{1-x}\text{O}/\text{Ti}$ electrode; first-principles calculation; electric collector; photoelectric synergistic catalysis

1. Introduction

It was estimated that 15% of untreated organic dyes widely used in various fields have been discharged into water directly [1, 2]. Those dyes could exist in ecosystem stably, devastate its self-degradation ability and make people suffer higher risk of intoxication, mutation and cancerization. Therefore, how to degrade organic dyes cost-effectively has become a hot topic [3-6]. One of the most widely studied method would be the semiconductor material-based PC technology. And ZnO, an atoxic direct band gap semiconductor with a wide band gap of 3.37 eV and an exciton binding energy of 60 mV, has been considered as one of the most ideal materials for wastewater treatment due to its excellent PC activity, great physical and chemical stability as well as high cost efficiency [7, 8]. It has been reported that compared with TiO₂, ZnO exhibited higher PC efficiency in terms of the degradation of several organic contaminants in both acidic and basic medium [9, 10]. However, the high recombination rate of photogenerated electron-hole pairs and oversized band gap have significantly limited its application. Hence, how to reduce the recombination rate and enlarge the light-absorption area have received much attention [11, 12].

In recent years, an external bias potential placed between the anode and cathode has proven an effective method to promote the electron-hole separation rate [13-15]. Under its effect, the aforementioned recombination rate was reduced, and more electrons and holes were allowed to participate in the reaction of oxidative cracking of organic dye as the photogenerated electrons were forced to move to the counter electrode through an external circuit, while the holes remained in the valence band thanks to the external electric field. In addition, Shaoce et al. designed a dual cocatalysts for spatial separation, of which Co-Pi as the outmost hole-transfer

layer and Pt as the bottom electron collector and transport layer, thereby photogenerated electrons-holes pairs were separated effectively and twice higher current density was obtained [12]. However, neither the external bias potential nor the electron collector could increase the yield of photogenerated electron-hole pairs, the light-absorption range was still relatively narrow. An efficient way to solve that problem was doping metal or non-metal elements into materials and change their electronic structure and band gap [16-19]. Ashebir et al. reported that both Mn- and Ag-doped ZnO nanoparticles showed a decreased band gap and higher PC performance relative to pure ZnO [20]. According to Qiu et al. who studied the effect of N-doping on the PC performance of ZnO, the forbidden band width decreased significantly and the PC activity was enhanced after the N 2p impurity energy level appeared [21]. Doping could also change the microstructure of the material [19, 22]. Vinodkumar et al. revealed that Mg-doped ZnO exhibited a significant c-axis compression and decreased grain size, its specific surface area was twice as large as that of pure ZnO [23].

In general, the bias potential and electron collector could reduce the recombination rate of photogenerated electron-hole pairs effectively, doping could expand the light-absorption area and change the material's microstructure. Given the fact that noble metal oxide RuO_2 is an excellent electrocatalyst with high conductivity [24-26], that the atomic radius disparity between Ru^{4+} and Zn^{2+} is smaller than 7% making it possible to prepared Ru-doped ZnO, and that the minute difference in electronegativity between the two atoms helps form solid solutions with greater solubility [27, 28], we finally chose Ru to modify ZnO and analyzed its impact on the electronic structure and the PEC performance of composite-oxide electrodes.

2. Experimental and calculation methods

2.1 Preparation of $\text{Ru}_x\text{Zn}_{1-x}\text{O}/\text{Ti}$ electrodes

Pretreatment of the Ti plates: in order to strengthen the bonding force between the substrate and the coatings, enlarge the surface area and extend the service life of the electrodes, the sandblasted $20 \times 20 \times 1.5$ mm TA2 titanium plate was degreased, etched in 10wt% H_2SO_4 for 2 h, then were cleaned with deionized water and preserved in absolute alcohol for further use.

Preparation of $\text{Ru}_x\text{Zn}_{1-x}\text{O}/\text{Ti}$ electrodes: the precursors $\text{RuCl}_3 \cdot x\text{H}_2\text{O}$ (containing 37% Ru by mass) and ZnCl_2 were used to prepare the mixed solutions with Ru contents of 0, 3.125, 6.25, 9.375 and 12.5mol% respectively, which were stirred evenly by ultrasonic vibration. Then an appropriate amount of the mixed solution ($3 \mu\text{l cm}^{-2}$) was brushed on the Ti plates, which were cured under an infrared lamp at $100 \text{ }^\circ\text{C}$ for 10 min, and pre-oxidized in a muffle furnace at $500 \text{ }^\circ\text{C}$ for another 10 min, followed by air cooling. After repeating those steps for six times, the samples were annealed at $500 \text{ }^\circ\text{C}$ for 60 min then cooled in the air, and the $\text{Ru}_x\text{Zn}_{1-x}\text{O}/\text{Ti}$ electrodes with different Ru contents were prepared.

2.2 Characterization techniques

The microstructures of the $\text{Ru}_x\text{Zn}_{1-x}\text{O}/\text{Ti}$ electrodes were observed by Scanning electron microscope (SEM, Supra 55, Carl Zeiss, Oberkochen, Germany) and Transmission electron microscope tests (TEM, TECNAI G2 F20, FEI, America). The phase structures of the coatings were studied by X-ray diffractometer test (XRD, Ultima III, Rigaku, Tokyo, Japan) with $\text{Cu K}\alpha$ radiation source and Ni filter, where the tube voltage and current were 36 kV and 30 mA, the angle range and scanning rate were $25\text{-}60^\circ$ and $2^\circ/\text{min}$ respectively. X-ray photoelectron spectroscopy (XPS) spectra were performed on the photoelectron spectroscopy system (Escalab

250, Thermo Scientific, America), and the elemental peak fitting was performed via the Avantage software. The UV-vis diffuse reflectance spectra (DRS) were tested through the UV2600 instrument with a wavelength range of 200-800nm. Specific surface areas (SSA) were tested with the Micromeritics 3Flex specific surface analyzer, the samples were degassed at 200 °C for 10 h.

2.3 First-principles calculations

According to the solid solution theory, both an ionic radius difference within 15% (Ru^{4+} 0.62 Å vs Zn^{2+} 0.74 Å) and minute electronegativity disparity (Ru 2.20, Zn 1.65) are favorable factors, indicating the high possibility of forming $\text{Ru}_x\text{Zn}_{1-x}\text{O}$ solid solution. Given that the ideal ZnO possesses a hexagonal wurtzite structure with a space group of P6₃/mc, a $2 \times 2 \times 2$ supercell structure model with 64 atoms was constructed, in which a small number of Zn and Ru atoms exchanged places, as shown in Fig. 1. In this study, VASP software was adopted to calculate the electronic structure of the Ru-doped ZnO crystal based on the plane-wave density functional theory (DFT), where the k-point meshes of the Brillouin zone were obtained via $9 \times 9 \times 5$ Monkhorst-Pack grid and the plane wave cut-off energy was 520 eV.

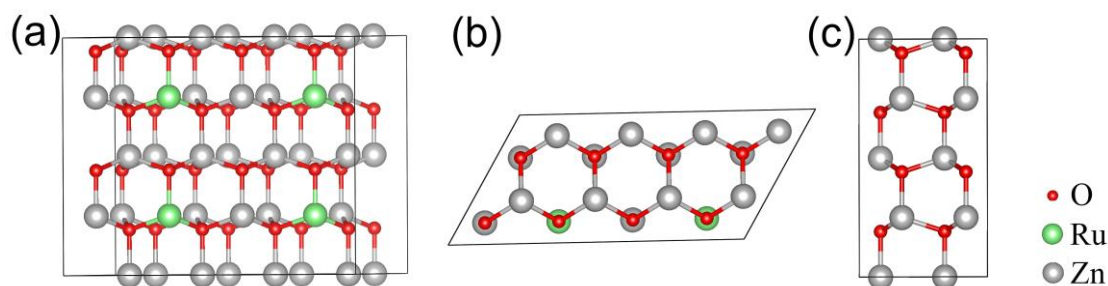


Fig. 1 Ru-doped ZnO with hexagonal wurtzite crystal structure (a) front view; (b) top view; (c) left view.

2.4 Electrochemical measurements

Electrochemical tests were performed with a three-electrode system via the Metrohm AUTOLAB Electrochemical Workstation (AUT84638, PGSTAT302N). Where the 0.1 M

Na₂SO₄ solution was adopted as the electrolyte, and the working, reference and counter electrodes were Ru_xZn_{1-x}O/Ti ones with different Ru contents, the saturated calomel electrode (SCE) and the large-area titanium plate respectively. The amplitude for electrochemical impedance spectroscopy test (EIS) was 10 mV and the frequency range was 0.05-10⁵ Hz. The linear sweep voltammetric (LSV) tests were performed with a potential range of 0-2.5 V and a scanning rate of 10 mV s⁻¹.

2.5 Photoelectrocatalytic degradation of RhB

The PEC performance of the Ru_xZn_{1-x}O/Ti electrodes was evaluated by the degradation rate of RhB. The experiment was conducted with a three-electrode configuration in a 500 mL cylindrical quartz beaker containing the mixed solution of 0.1 M Na₂SO₄ and 20 mg L⁻¹ RhB. In which, a 100 W ultraviolet mercury lamp (386 nm) was placed directly opposite the working electrode with a surface area of 4 cm², and the light intensity (15 mW cm⁻²) was monitored via a light intensity photometer (UV-M10-P/S, ORC, Japan). The solution was continuously stirred, and the potential was 2.5 V. The removal rate of RhB during each degradation period was evaluated via a Cary 50 UV-vis spectrophotometer (varian) and the total organic carbon (TOC) tests were carried out through Shimadzu TOC-L ASI-L.

3. Results and discussion

3.1 Microstructure morphology analysis

As we could see from the SEM images of the Ru_xZn_{1-x}O/Ti electrodes with different Ru contents shown in Fig. 2., the coating surface exhibited both large and small typical hexagonal prism ZnO grains [12, 29]. According to Fig. 2 (a), ZnO nanorods on the surface of pure ZnO coatings arranged orderly, possessing a relatively larger crystal grain diameter of 0.1-1 μm.

However, as Ru content increased, ZnO nanorods tended to grow disorderly and the diameter gradually decreased with a few exceptions. I.e., adding Ru could reduce the grain size of ZnO, increase the irregularity degree of coatings, and thus enlarge the specific surface area.

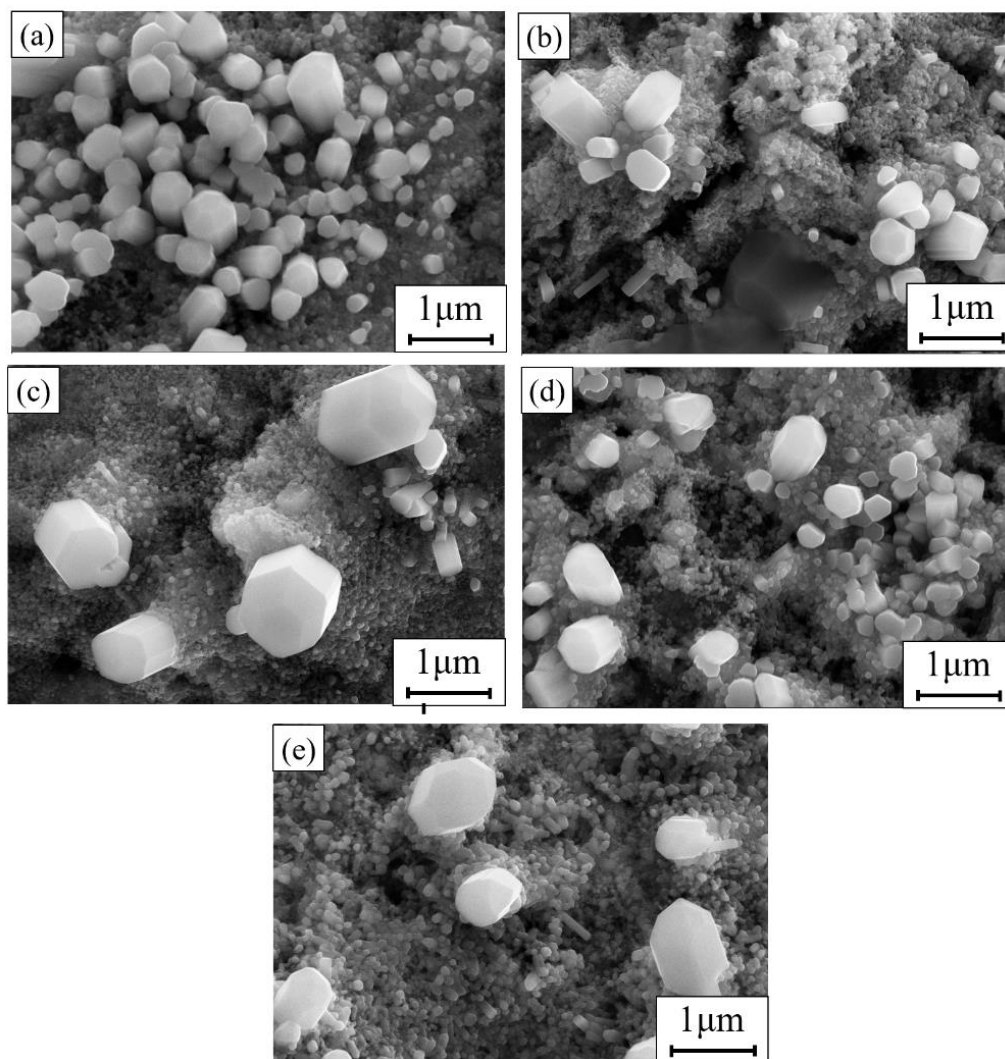


Fig. 2 SEM images of $\text{Ru}_x\text{Zn}_{1-x}\text{O}/\text{Ti}$ electrodes (a) 0mol%; (b) 3.125mol%; (c) 6.25mol%; (d) 9.375mol%; (e) 12.5mol%.

Phase analysis of the $\text{Ru}_x\text{Zn}_{1-x}\text{O}/\text{Ti}$ electrodes were carried out through the XRD tests. Pure ZnO electrodes only exhibited the diffraction peak of hexagonal wurtzite phase ZnO (space group: P63/mc, JCPDS 36-1451) as displayed in Fig. 3 (a). By contrast, those $\text{Ru}_x\text{Zn}_{1-x}\text{O}/\text{Ti}$ ones showed not only the diffraction peaks of ZnO, but the tetragonal phase of RuO_2 (space group: P42/mnm, JCPDS 18-1139) and metal Ru (JCPDS 06-0663). The relatively sharper peak

of ZnO indicated a higher degree of crystallization. The grain size of ZnO was calculated by the following Scherrer equation (applied to the (101) crystal plane) [30]:

$$D = \frac{k\lambda}{\beta \cos \theta} \quad (1)$$

Where k is the Scherrer constant ($=0.89$), λ is the X-ray wavelength of Cu $K\alpha$ ($=0.154\text{nm}$), β is the full width at half maximum (FWHM) of the (101) crystal plane diffraction peak of ZnO, and θ is the diffraction angle. According to the results shown in Table 1, the grain size of ZnO decreased from 33 nm to 26 nm with the increase of Ru contents, coinciding with the SEM analysis [23, 31-33]. As shown in Fig. 3 (b), the 2θ angles of 31.769° , 34.421° , and 36.252° corresponded to the (100), (002), and (101) crystal planes of hexagonal wurtzite phase ZnO respectively. Compared with pure ZnO, the 2θ of the three diffraction peaks of Ru-doped ones shifted to a higher angle, the higher the Ru contents, the larger the deviation degree, indicating that $\text{Ru}_x\text{Zn}_{1-x}\text{O}$ solid solution was formed after a number of Zn^{2+} in the ZnO lattice were replaced by Ru^{4+} with smaller radius [32, 34, 35].

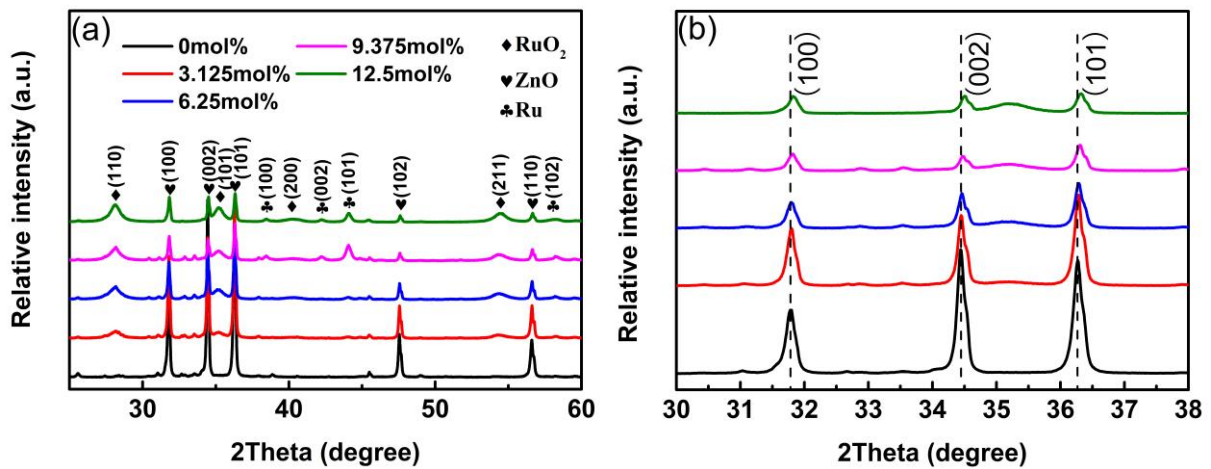


Fig. 3 XRD patterns of $\text{Ru}_x\text{Zn}_{1-x}\text{O}/\text{Ti}$ electrodes (a) 2θ within $25\text{-}60^\circ$; (b) enlarged view of 2θ within $30\text{-}38^\circ$.

Table 1The grain size of Ru_xZn_{1-x}O/Ti coatings

The content of Ru ⁴⁺ (mol%)	0	3.125	6.25	9.375	12.5
Grain size (nm)	33	30	29	28	26

According to the results listed in Table 2, the SSA of the of Ru_xZn_{1-x}O/Ti electrodes increased gradually as the Ru content rose as adding Ru could reduce the grain size of ZnO nanorods and increase coatings' irregularity degree, which helped provide more active sites for PEC degradation.

Table 2The SSA of Ru_xZn_{1-x}O/Ti coatings

The content of Ru ⁴⁺ (mol%)	0	3.125	6.25	9.375	12.5
SSA (m ² g ⁻¹)	1.536	1.881	2.909	4.077	7.422

The microstructures of the Ru_xZn_{1-x}O/Ti electrodes were analyzed by TEM test. Fig. 4 (a, b) revealed that the wurtzite-type ZnO nanorods were piled up by the (001) planes, coinciding with its single-crystal characteristic [29]. The SAED pattern shown in Fig. 4 (c) further confirmed that feature and the three diffraction spots corresponded to the (101), (100) and (002) crystal planes of ZnO respectively. According to Fig. 4 (d), the RuO₂ nanoparticles distributed on the ZnO nanorods' surface uniformly, this structure facilitated the transfer of electrons and the separation of photo-generated electrons and holes. The lattice spacing of 0.248 nm and 0.317 nm displayed in Fig. 4 (e), corresponded to the (101) crystal plane of ZnO (JCPDS 36-1451) and the (110) crystal plane of RuO₂ (JCPDS 18-1139) respectively. Fig. 4 (f) exhibited the polycrystalline electron diffraction pattern of ZnO and RuO₂, where the two diffraction spots corresponded to the (101) crystal planes of ZnO and the (110) crystal plane of RuO₂ respectively, consistent with the XRD analysis.

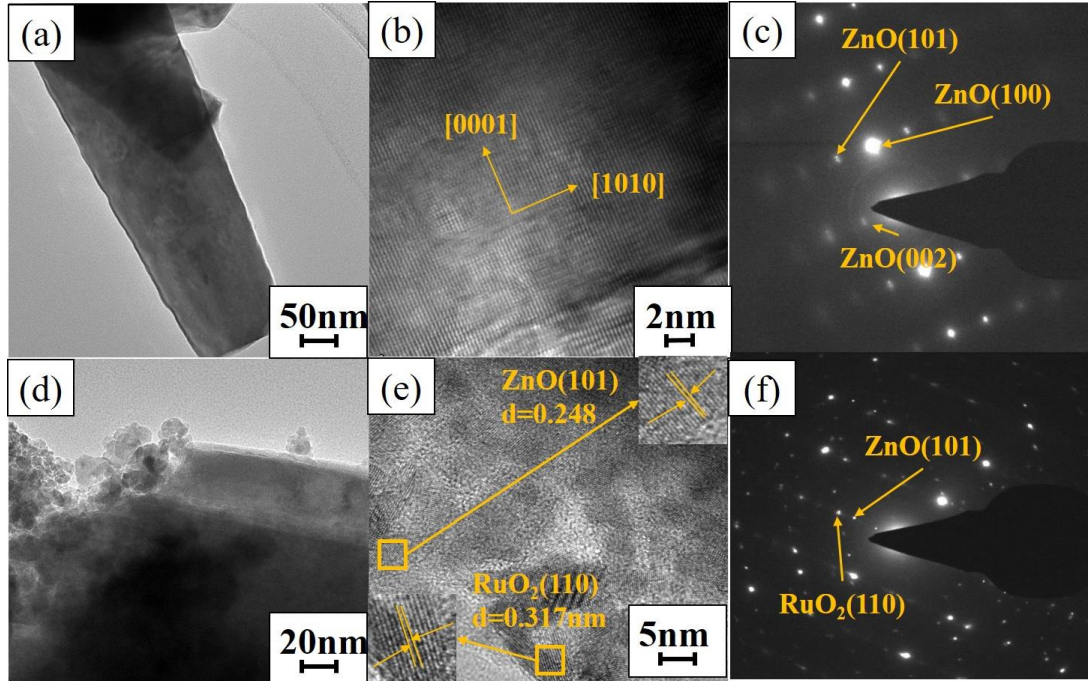


Fig. 4 TEM and SAED patterns of $\text{Ru}_x\text{Zn}_{1-x}\text{O}/\text{Ti}$ electrodes (a, b, c) 0mol%; (d, e, f) 9.375mol%.

X-ray photoelectron spectroscopic analysis of $\text{Ru}_x\text{Zn}_{1-x}\text{O}/\text{Ti}$ electrodes was carried out to identify the elements' composition and valence and the results were adjusted with C1s 284.8 eV. According to the Fig. 5 (a), the full spectra of $\text{Ru}_x\text{Zn}_{1-x}\text{O}/\text{Ti}$ electrodes have exhibited all the characteristic peaks of Ru3d, Zn2p, O1s and C1s. The high-resolution narrow scan spectra of Ru3d shown in Fig. 5 (b), displayed a pair of narrow characteristic peaks, corresponding to the two spin-orbital components of Ru3d_{5/2} and Ru3d_{3/2} respectively, which located at 280.48 eV and 284.98 eV with a spin separation energy of 4.5 eV when the Ru content was 9.375mol% [36-38]. The Ru3d characteristic peaks could be divided into 5 ones, coinciding with the three existing forms of Ru (RA for Ru, RB for RuO_2 and RC for RuO_x/Ru) and C element. Where peaks at 280.66 eV and 284.91 eV corresponded to Ru^{4+} in RuO_2 , obtained by heat treatment after the coatings were exposed to the surrounding environment. The one located at 280.45 eV was consistent with the zero valence of Ru^0 , resulting from the disproportionation of RuCl_3 or the insufficient oxygen supply during the heat treatment. The peak at 282.05eV indicated the

existence of RuO_x/Ru anoxic ruthenium, and the peak of C1s appeared at 284.8eV [38-40]. As shown in Table 3, compared with the electrodes with 9.375mol% Ru, the Ru3d characteristic peak of those containing 12.5mol% Ru red-shifted by 0.12 eV, as the RuO₂ content decreased and the RuO_x/Ru content increased [41]. The high-resolution narrow scan spectra of Zn2p in Fig. 5 (c) exhibited two spin orbits, Zn2p_{3/2} and Zn2p_{1/2}, with a spin separation energy of 23 eV. Pure ZnO electrodes displayed double peaks of Zn2p_{3/2} and Zn2p_{1/2} at 1021.41 eV and 1044.42 eV respectively, corresponding to Zn²⁺ in ZnO [23, 42]. Besides, those peaks blue-shifted by 0.42 eV and 0.70 eV, when the Ru content was 9.375mol% (1021.83 eV and 1044.85 eV) and 12.5mol% (1022.11 eV and 1045.13 eV) respectively, due to the replacement between Zn²⁺ and Ru⁴⁺. After the formation of Zn-O-Ru bond, the electron density around Zn atoms reduced as the electronegativity of Ru (2.20) was greater than that of Zn (1.65). Accordingly, the binding energy between the nucleus and extranuclear electrons of Zn atoms was strengthened, while that of Ru atoms was weakened, which was also one reason for the red shift of Ru3d characteristic peak [23, 43, 44]. The high-resolution narrow scan spectra of O1s were shown in Fig. 5 (d), where the O1s characteristic peaks of pure ZnO electrode could be divided into two, the peak located at 531.70 eV resulted from adsorbed O₂ or OH⁻ ions, while the one at 530.02eV corresponded to O²⁻ in ZnO. By contrast, other than the aforementioned peaks, electrodes containing Ru exhibited another O1s characteristic peak at 529.40 eV, coinciding with O²⁻ in RuO₂.

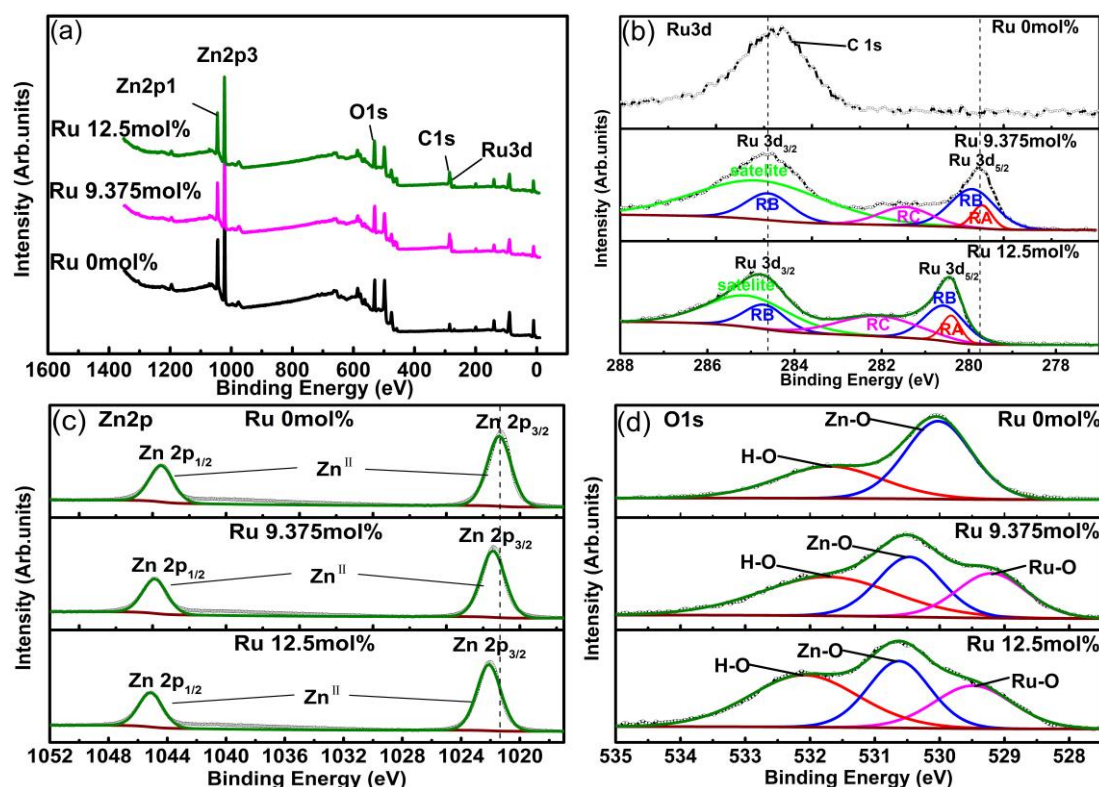


Fig. 5 XPS spectra of $\text{Ru}_x\text{Zn}_{1-x}\text{O}/\text{Ti}$ coatings (a) full spectra; (b) Ru 3d; (c) Zn 2p; (d) O 1s.

Table 3

Peak position and corresponding peak area ratio of XPS spectra of high-resolution Ru3d and Zn2p

Atomic (%)	Orbital/spin	Peak position (eV)	Area under peak (%)	
			Ru 9.375mol%	Ru 12.5mol%
Ru	$3d_{5/2}$	280.2 ± 0.2	0.90	1.36
RuO_x/Ru	$3d_{5/2}$	281.9 ± 0.2	1.88	5.64
RuO_2	$3d_{5/2}$	280.9 ± 0.2	5.73	4.72
ZnO	$2P_{3/2}$	1021.8 ± 0.2	91.49	88.28

3.2 Band structure and density of state analysis

The effect of Ru contents on the electronic structure of $\text{Ru}_x\text{Zn}_{1-x}\text{O}$ solid solution was analyzed by the first-principles calculation, the band and crystal structure characteristics were also explained in detail. According to the data listed in Table 4, the calculated results of this study were very close with other research's. The lattice parameters a , c and unit cell volume (V_0) of the solid solution all decreased with the increase of Ru content as the ionic radius of Ru

(0.69 Å) was smaller than that of Zn (0.74 Å) [27, 45]. The band structure and density of state (DOS) of $\text{Ru}_x\text{Zn}_{1-x}\text{O}$ solid solution was shown in Fig. 6. Typically, the Fermi level is close to the central portion of the forbidden band [46]. As reflected in Fig. 6 (a), the minimum calculated energy gap (E_g) of pure ZnO samples was about 1.78 eV, though smaller than the experimental value (3.37 eV), the result was still competitive with previous studies by Rafael [47] (1.87 eV) and Bendavid [45] (1.90 eV). A possible reason was that the DFT theory did not take strong coulomb correlation and interaction between electrons into consideration, leading to an underestimated band gap value. As shown in Fig. 6 (a-e), after adding Ru, the conduction band of ZnO moved down, the valence band moved up, and the impurity level appeared and narrowed the band gap. The higher the Ru contents, the narrower the band gap (1.44 eV for 3.125mol%, 0.72 eV for 6.25mol%, 0.39 eV for 9.375mol%, 0.24 eV for 12.5mol%). In other words, the addition of Ru had a significant effect on the band structure of ZnO, reduced the electron-transfer energy barrier. According to the DOS of the $\text{Ru}_x\text{Zn}_{1-x}\text{O}$ electrodes shown in Fig. 6 (f-j), pure ZnO samples exhibited peaks in four areas: peaks nearby -19 eV were mainly caused by the O2s orbit, those appeared within the range of -9.5 to -7.5 eV and -6.5 to -1.5 eV were resulted from the hybridization of O2p and Zn3d orbits, and peaks located at the conduction band of about 8 eV were mainly formed by Zn4s and O2p. A significant difference in the electronic structure between Ru-doped and pure ZnO samples was that an impurity level appeared in the forbidden bands and narrowed the band gap, due to the electronic states of Ru4d. As the Ru content increased, more electron energy levels appeared near the Fermi level, the electrons became more active and the conductivity was enhanced accordingly. However, with the band gap narrowing down, the recombination rate of photogenerated electron-hole pairs

also increased.

Table 4

Comparison of calculated and experimental values of parameters (a and c) and lattice volume (V_0) of

$\text{Ru}_x\text{Zn}_{1-x}\text{O}/\text{Ti}$ solid solution

	A (Å)	C (Å)	α, β, γ (°)	V_0 (Å ³)	References
ZnO	3.250	5.207	90,90,120	47.600	JCPDS 36-1451
	3.250	5.232	90,90,120	----	Cal. [48]
	3.252	5.222	90,90,120	----	Cal. [49]
0mol%	3.249	5.145	90,90,120	46.900	This work
3.125mol%	3.242	5.136	89.968,90,120.209	46.348	This work
6.25mol%	3.232	5.098	89.995,90,120.017	46.263	This work
9.375mol%	3.226	5.077	89.018,90.888,121.171	46.200	This work
12.5mol%	3.224	5.055	88.392,91.499,121.249	46.168	This work

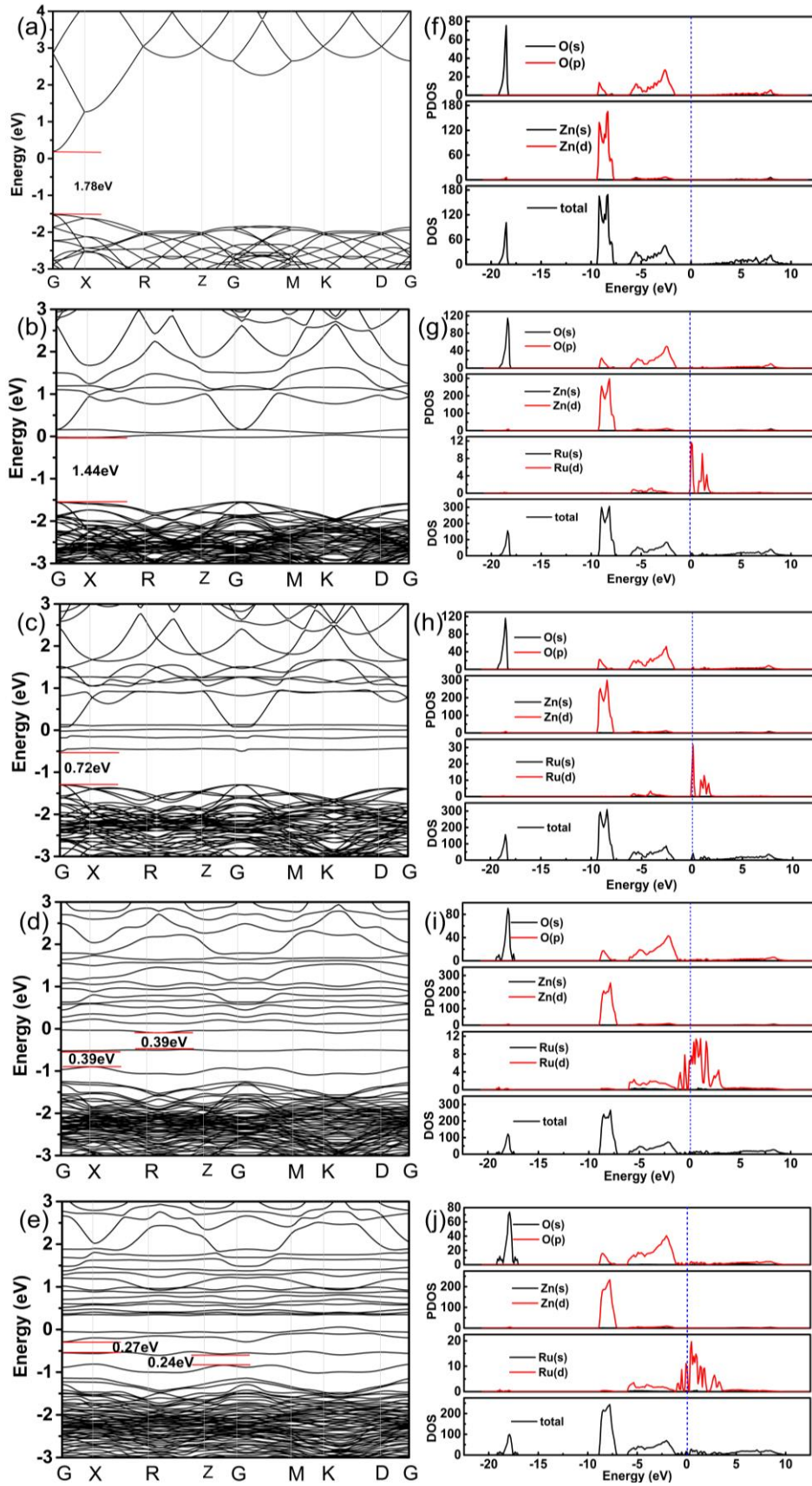


Fig. 6 Band structure and density of state of the $\text{Ru}_x\text{Zn}_{1-x}\text{O}$ solid solution (a, f) 0mol%; (b, g) 3.125mol%; (c, h) 6.25mol%; (d, i) 9.375mol%; (e, j) 12.5mol%.

The UV-DRS tests were performed to observe the forbidden band width of the $\text{Ru}_x\text{Zn}_{1-x}\text{O}/\text{Ti}$ coatings and the value was calculated through the following Tauc-plot method [50]:

$$\alpha h\nu = A(h\nu - E_g)^{1/n} \quad (2)$$

Where α is the absorbance index, h is the Planck constant, ν is the frequency, constant A represents the slope of the Tauc edge, n equals to $1/2$, determined by the semiconductor type, and E_g is the band gap, reflected by the intersection point of the linear part of the curve of $(\alpha h\nu)^2$ and the $h\nu$ axis. According to the results shown in Fig. 7, the band gap (3.12 eV) of pure ZnO was slightly smaller than the theoretical value (3.37 eV) because of the lack of oxygen [51]. Besides, the band gap decreased with the increase of Ru contents, coinciding with the theoretical calculation results.

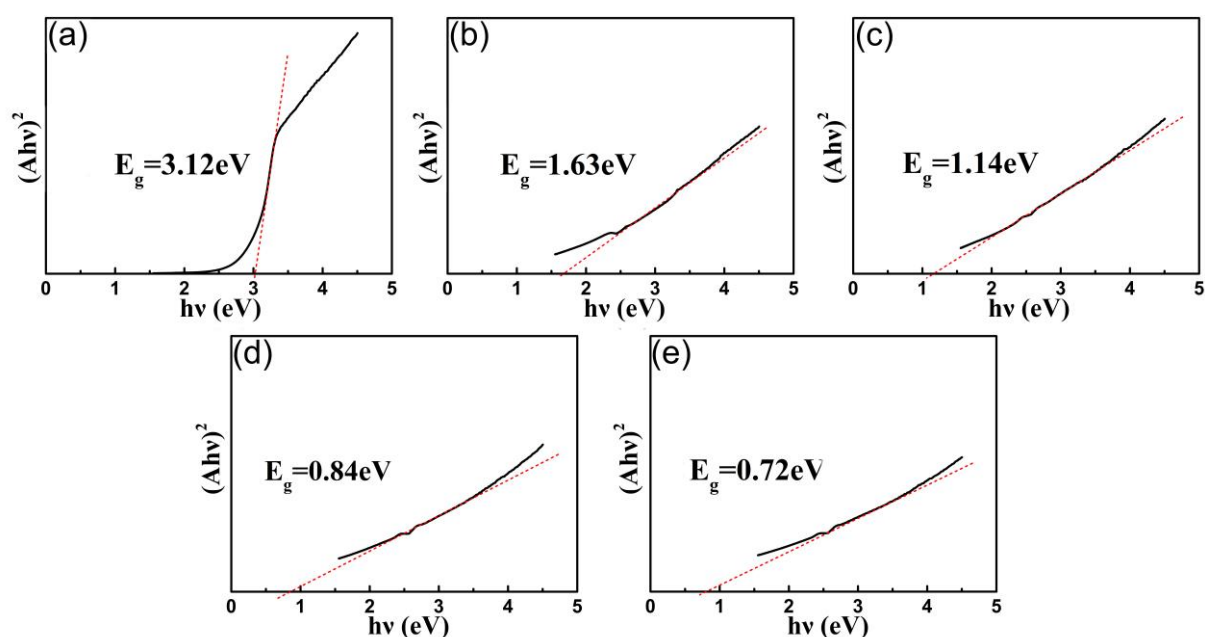


Fig. 7 The UV-DRS patterns of the $\text{Ru}_x\text{Zn}_{1-x}\text{O}/\text{Ti}$ coatings (a) 0mol%; (b) 3.125mol%; (c) 6.25mol%; (d) 9.375mol%; (e) 12.5mol%.

3.3 Electrochemical measurements

As shown in Fig. 8, the LSV test of the $\text{Ru}_x\text{Zn}_{1-x}\text{O}/\text{Ti}$ electrodes without (a) and with UV

irradiation (b) were performed at a scanning rate of 10 mV s^{-1} . It could be seen that when the potential exceeded 1.6 V, the current densities increased rapidly thanks to the electrolyzed water. With the rise of Ru contents, the current densities increased first, then decreased, with or without UV irradiation, and reached the maximum when the content was 9.375mol%. This was partly because pure ZnO coatings had a relatively larger band gap and poorer conductivity, leading to a lower current density when voltage remained the same. With the addition of Ru, coatings' band gap decreased and the conductivity was improved, resulting in an increased number of active photo-generated electron-hole pairs and enhanced current density. However, with a Ru content of 12.5mol%, excessive RuO_2 particles would pile up on ZnO nanorods' surface, narrowing its effective light-sensitive area. Besides, the narrowed band gap also resulted in an increased electron-hole recombination rate. As we could see from Fig. 8 (a, b), samples under UV irradiation exhibited stronger current densities due to the generation of photocurrent.

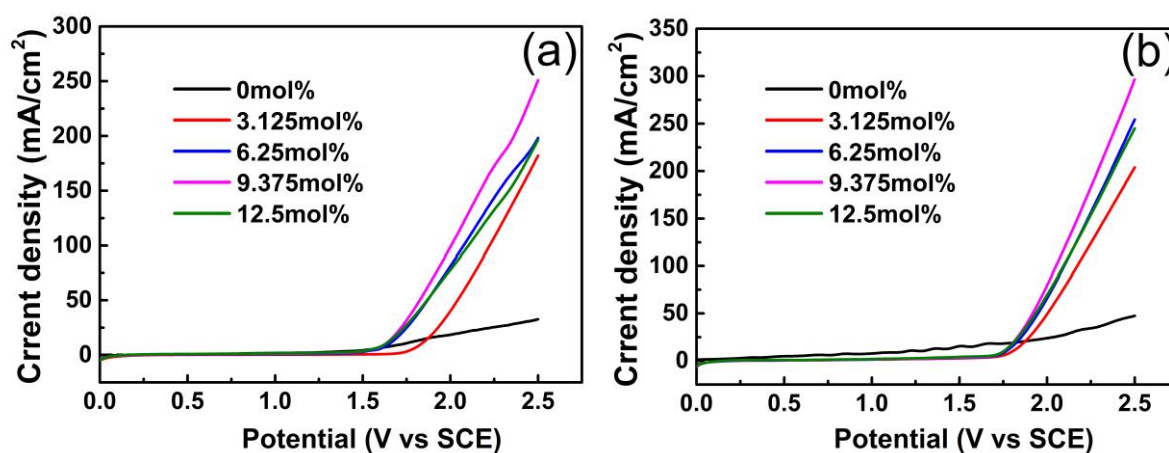


Fig. 8 The LSV curves of the $\text{Ru}_x\text{Zn}_{1-x}\text{O}/\text{Ti}$ electrodes (a) without UV irradiation; (b) with UV irradiation.

Fig. 9 (a) showed the Nyquist plots of the $\text{Ru}_x\text{Zn}_{1-x}\text{O}/\text{Ti}$ electrodes, and the enlarged view of its high frequency region displayed in Fig. 9 (c), where points and lines referred to the experimental and fitted data respectively. Fig. 9 (b) exhibited the equivalent circuit, in which L represented the inductive reactance of the electrochemical system, R_s referred to the

intersection of the high frequency region and the real axis, reflecting the sum of the solution resistance and the coatings' internal resistance, R_f and R_{ct} indicated the coating-substrate or coating-electrolyte resistance and the faraday transfer resistance respectively, Z_w was the Warburg impedance, representing the ionic diffusion process taking place on the interface between the electrodes and electrolyte. Q reflected a constant phase angle element, and C_{dl} referred to the double-layer capacitance [52-54]. According to the results, R_s decreased all the way as the Ru content increased, indicating a reduced internal resistance. The diameter of the semicircle curve in the high-frequency region reflected the charge-transfer resistance, which decreased first, then increased and reached to the minimum when the Ru content was 9.375mol%, suggesting the electrodes' highest separation rate and transfer efficiency. As shown in Fig. 9 (d), compared with the impedance spectrum of electrodes without UV irradiation, those under the light exhibited a larger inclination degree at the low frequency region, indicating that the UV irradiation accelerated the ion-diffusion rate.

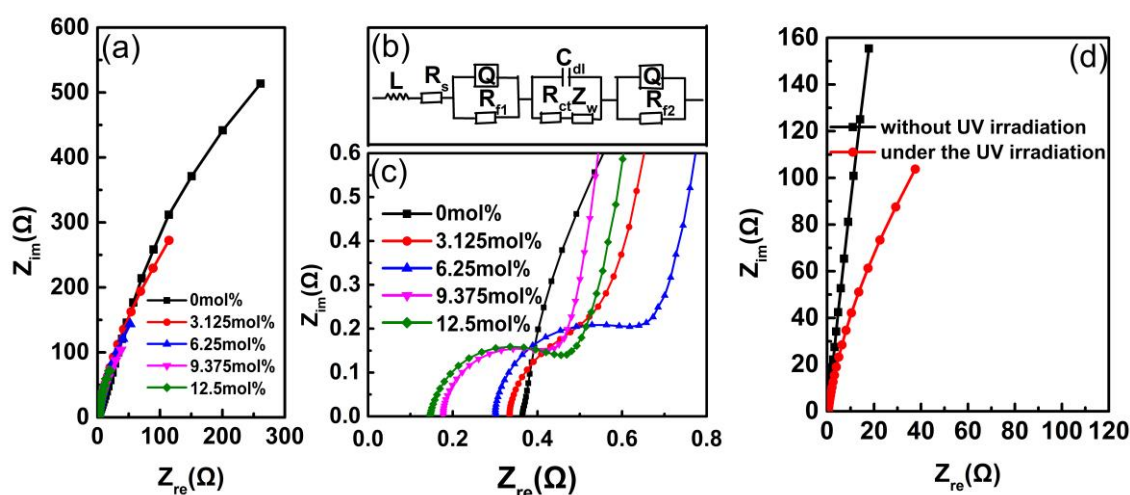


Fig. 9 (a) Nyquist plots of the $Ru_xZn_{1-x}O/Ti$ electrodes; (b) the electrical equivalent circuit for the fitting of the impedance spectra; (c) the enlarged view of the high frequency region of the Nyquist plots; (d) the Nyquist plots with and without UV irradiation.

3.4 Photoelectrocatalytic degradation of RhB

As we could see from the UV-vis absorption spectra and the removal rate of RhB during PEC degradation process exhibited in Fig. 10 (a-f), the strongest absorption peak of RhB located at 554 nm. And the peaks' intensity decreased as the degradation time increased, the one corresponding to the electrode with 9.375mol% Ru disappeared first. According to Fig. 10 (f), as the Ru content rose, the removal rate increased first, from 71% of the pure ZnO electrode (120min), then decreased after reaching to the maximum of 97% (electrode containing 9.375mol% Ru), indicating that doping appropriate amount of Ru could significantly improve electrodes' degradation efficiency. The TOC test results shown in Fig. 10 (g) confirmed that the addition of Ru could improve the TOC removal rate effectively, which exhibited an inverted U-shaped curve and reached to the maximum of 68% when the Ru content was 9.375mol%. This was partly because the shortage of wide forbidden band of pure ZnO coatings and related problems including relatively smaller light-sensitive area and lower yield of photogenerated carriers could be overcome by adding Ru. Meanwhile, the RuO₂ particles growing on ZnO surface provided an efficient electron-transfer channel and reduced the recombination rate of photogenerated electron-hole pairs. And the coatings' surface became less smooth with the addition of Ru, providing more active sites. However, with a Ru content of 12.5mol%, excessive RuO₂ particles wrapped around ZnO surface, hindering the irradiation of ultraviolet light. Though the forbidden band width of ZnO decreased after adding Ru, undersized band gap could accelerate the recombination rate of photogenerated electron-hole pairs in turn. That explained why the electrodes containing 9.375mol% Ru exhibited the highest degradation rate.

In order to further illustrate the effect of Ru content on the degradation rate, the

degradation kinetic analysis was carried out under the direction of the following first-order kinetic equation [55]:

$$-\ln\left(\frac{C_0}{C}\right) = kt \quad (3)$$

Where C_0 is the initial concentration of the RhB solution (20 mg L^{-1}), C is the concentration of RhB for a given degradation time, k is the reaction rate constant (min^{-1}), and t is the reaction time. As the Ru content rose, k value increased first, then decreased, and reached to the maximum of 0.03 when the content was 9.375mol%, indicating the electrodes' highest removal rate.

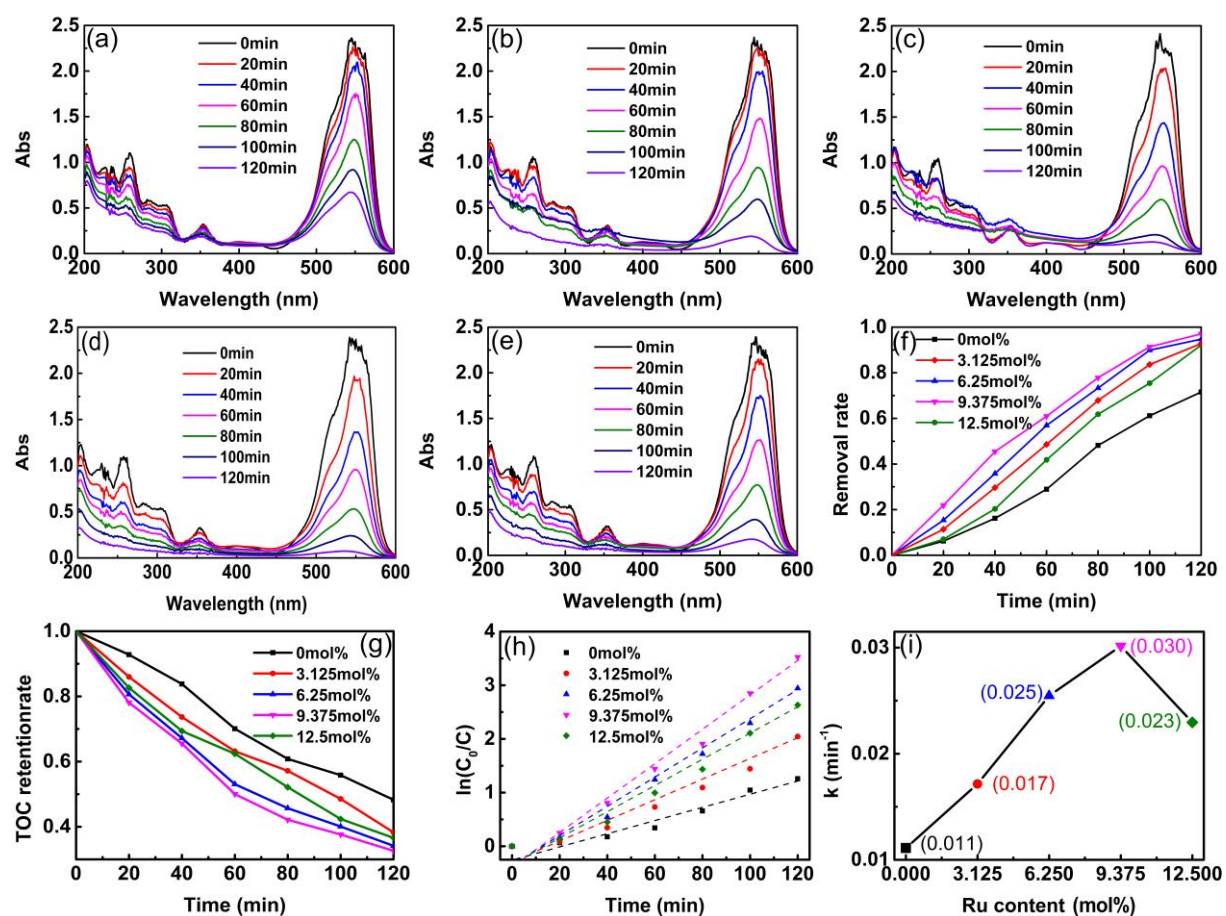


Fig. 10 UV-vis absorption spectra of $\text{Ru}_x\text{Zn}_{1-x}\text{O}/\text{Ti}$ electrodes under PEC degradation with different intervals (a) 0mol%; (b) 3.125mol%; (c) 6.25mol%; (d) 9.375mol%; (e) 12.5mol%; along with (f) removal

ratio of RhB; (g) removal ratio of TOC; (h) degradation kinetics; (i) the reaction rate constant.

To make further explanation, the PC and EC degradation tests of $\text{Ru}_x\text{Zn}_{1-x}\text{O}/\text{Ti}$ electrodes containing 9.375mol% Ru were also performed respectively, and the results were shown in Fig. 11. With a degradation time of 120 min, the removal rates of EC, PC and PEC were 12%, 50%, and 97% respectively, the much higher PEC efficiency confirmed the synergy effect of EC and PC degradation. According to the test results displayed in Fig. 11 (g), after 120 min of degradation, the TOC removal rates for PEC, PC, and EC were 68%, 44%, and 10%, respectively. Compared with EC, the photogenerated electron-hole pairs generated during PEC process, the holes could decompose RhB directly, and oxidize hydroxide ions on the electrodes' surface into hydroxyl radicals, which would oxidize RhB in turn. Compared with PC, PEC was provided with an external power source and the RuO_2 particles on the ZnO surface acting as an electro-transfer channel, offered more active sites for electrocatalysis and helped separate the photogenerated electron-hole pairs. In addition, a bias potential of 2.5 V facilitated the oxygen evolution reaction, providing the oxygen needed to oxidize RhB. It could be seen from Fig. 11 (e, f) that the regression curve basically accorded with first-order kinetics, and the rate constant of PEC (0.030 min^{-1}) was much larger than that of EC (0.001 min^{-1}) and PC (0.006 min^{-1}), confirming the synergy effect of PEC degradation again. As shown in Fig. 11 (h, i), the degradation rate of Ti plate was only 15.3% after 120 min, therefore, its effect on the $\text{Ru}_x\text{Zn}_{1-x}\text{O}/\text{Ti}$ electrodes' degradation rate could be ignored.

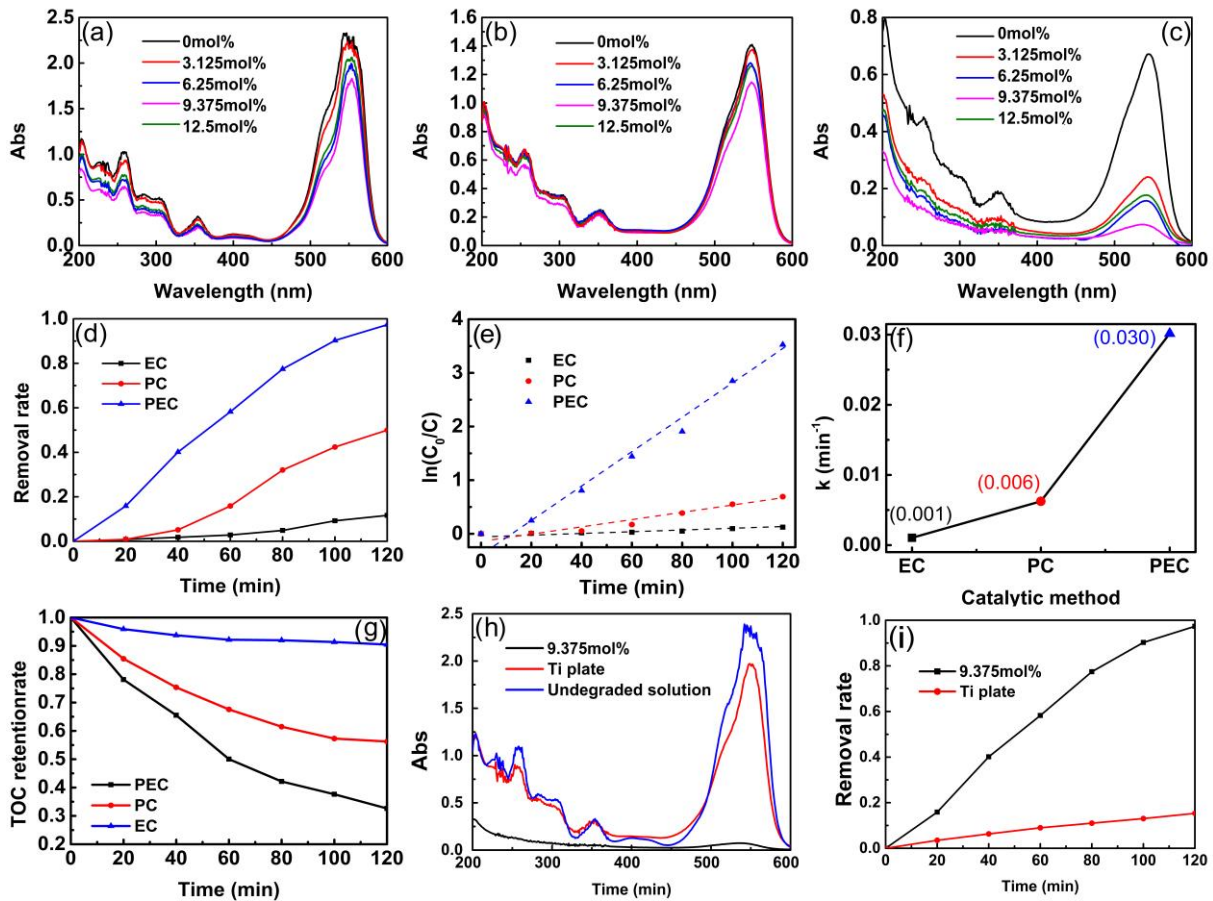
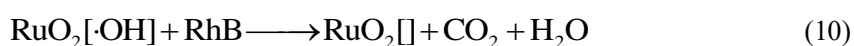
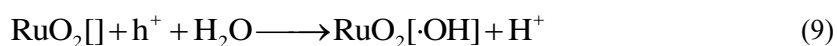
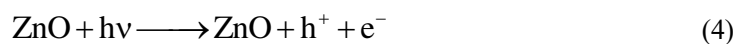


Fig. 11 UV-visible absorption spectra of $\text{Ru}_x\text{Zn}_{1-x}\text{O}/\text{Ti}$ electrodes containing of 9.375mol% Ru with different catalytic methods (a) EC; (b) PC; (c) PEC; (d) removal rates of PEC, PC and EC; (e) degradation kinetics; (f) reaction rate constant; (g) TOC removal rates of PEC, PC and EC; (h) Comparison UV-visible absorption spectra after 120 min degradation; (i) removal rates of electrodes containing 9.375mol% Ru and Ti plates.

3.5 Photoelectrocatalytic mechanism

The model shown in Fig. 13 could further illustrate the effect of Ru contents on ZnO nanorods in terms of the electron transfer and the mechanism of PEC degradation. It has been found that the photogenerated electron-hole pairs generated only when photons with energy of no less than the band gap were absorbed. To some extent, the large band gap of ZnO limited the number of photogenerated electron holes. However, the Ru-doped ZnO exhibited a conduction

band energy reduced from E1 to E3, while the valence band energy increased from E2 to E4, and the impurity energy level appeared in the band gap, which decreased the energy band width and expanded the light-absorption area. Besides, RuO₂ particles growing on ZnO nanorods' surface offered an efficient electron-transfer channel and more active sites [56, 57]. Together with the external power source, it could propel the photo-generated electrons to transfer towards the counter electrode, thus increased the separation rate of the photogenerated electron-hole pairs significantly. Furthermore, those electrons could react with molecular oxygen and generate superoxide radicals, which then reacted with hydrogen ions and generated hydroxyl radicals in turn [58]. Meanwhile, the holes could decompose the organic dyes directly, and oxidize hydroxide ions into hydroxyl radicals [59]. Together, those holes and hydroxyl radicals degraded RhB into harmless compounds such as H₂O and CO₂ [60, 61]. The following were specific chemical formulas:



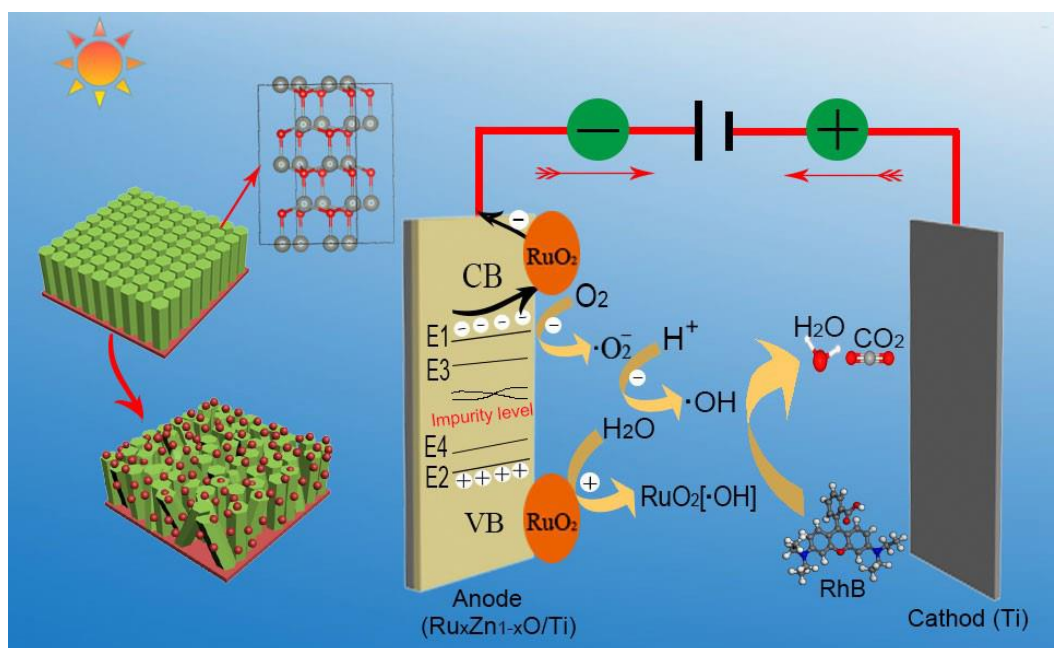


Fig. 13 Schematic microstructure model and PEC mechanism of $\text{Ru}_x\text{Zn}_{1-x}\text{O}/\text{Ti}$ electrodes.

4. Conclusion

$\text{Ru}_x\text{Zn}_{1-x}\text{O}/\text{Ti}$ electrodes with excellent PEC performance were prepared through simple thermal decomposition method. It has been found that Ru-doped ZnO exhibited a smaller forbidden band width as a number of Zn^{2+} and Ru^{4+} exchanged placed in ZnO lattice, and the amount of photogenerated carriers increased accordingly. The rest of Ru existed on ZnO nanorods' surface in the form of RuO_2 particles acting as an electron-transfer channel, together with the external bias, it propelled photogenerated electrons to transfer to the counter electrode and reduced the recombination rate of electron-hole pairs. Meanwhile, with the addition of Ru, the grain size of ZnO nanorods decreased and the coatings' surface became less smooth, leading to larger specific surface area as well as more active sites. The accessory oxygen evolution reaction could also accelerate the oxidation of the dye. However, with excessive Ru content, RuO_2 particles could wrap ZnO nanorods around and hinder the irradiation of ultraviolet light, reducing the PEC efficiency. Indeed, the band gap decreased with the addition of Ru, but

undersized band gap could accelerate the recombination rate of photogenerated electron-hole pairs. That explained why the electrodes with 9.375mol% rather than those containing 12.5mol% Ru exhibited the best PEC performance.

Acknowledgments

This research was completed with the support of the National Natural Science Foundation of China (83418083) and the Natural Science Foundation of Fujian Province (2019J01230).

References

- [1] Weber EJ, Adams RL. Chemical-mediated and sediment-mediated reduction of the azo-dye disperse-blue-79. *Environ Sci Technol* 1995, 29: 1163-1170.
- [2] Zhang FL, Zhao JC, Shen T, et al. TiO₂-assisted photodegradation of dye pollutants-II. Adsorption and degradation kinetics of eosin in TiO₂ dispersions under visible light irradiation. *Appl Catal B-Environ.* 1998, 15, 147-156.
- [3] Afzaal M, Malik MA, O'Brien P. Preparation of zinc containing materials. *New J Chem* 2007, 31, 2029-2040.
- [4] Kamat PV. Meeting the clean energy demand: Nanostructure architectures for solar energy conversion. *J Phys Chem C* 2007, 111, 2834-2860.
- [5] Roshan A, Joseph C, Ittyachen MA, Growth and characterization of a new metal-organic crystal: potassium thiourea bromid. *Mater Let* 2001, 49, 299-302.
- [6] Vayssieres L. Growth of arrayed nanorods and nanowires of ZnO from aqueous solutions. *Adv Mater* 2003, 15, 464-466.
- [7] Kumar SG, Rao K. Zinc oxide based photocatalysis: tailoring surface-bulk structure and related interfacial charge carrier dynamics for better environmental applications. *Rsc Advances* 2015, 5, 3306-3351.
- [8] Kim KJ, Kreider PB, Choi C, et al. Visible-light-sensitive n-doped p-type flower-like ZnO photocatalysts synthesized via a continuous flow microreactor. *Rsc Advances* 2013, 3, 12702-12710.
- [9] Lee JC, Park S, Park HJ, et al. Photocatalytic degradation of TOC from aqueous phenol solution using solution combusted ZnO nanopowders. *J Electroceram* 2009, 22, 110-113.
- [10] Khassin AA, Yurieva TM, Kaichev VV, et al. Metal-support interactions in cobalt-aluminum co-precipitated catalysts: XPS and CO adsorption studies. *J Mol Catal A-Chem* 2001, 175, 189-204.
- [11] Gomes YF, Freitas AK, Nascimento RM, et al. Experimental statistic design applied for obtaining Zn:Xce by microwave-assisted hydrothermal method with photocatalytic property. *J Adv Ceram* 2016, 5, 103-110.
- [12] Xiong Y, Tang ZL, Wang Y, et al. Gas sensing capabilities of TiO₂ porous nanoceramics prepared through premature sintering. *J Adv Ceram* 2015, 4, 152-157
- [13] Chai SN, Zhao GH, Li PQ, et al. Novel sieve-like SnO₂/TiO₂ nanotubes with integrated photoelectrocatalysis: Fabrication and application for efficient toxicity elimination of nitrophenol wastewater. *J Phys Chem C* 2011, 115, 18261-18269.
- [14] Wang X, Zhao HM, Quan X, et al. Visible light photoelectrocatalysis with salicylic acid-modified TiO₂ nanotube array electrode for p-nitrophenol degradation. *J Hazard Mater* 2009, 166, 547-552.
- [15] Dai GP, Yu JG, Liu G. Synthesis and enhanced visible-light photoelectrocatalytic activity of p-n junction BiOI/TiO₂ nanotube arrays. *J Phys Chem C* 2011, 115, 7339-7346.
- [16] Wang XQ, Zhou YN, Li R, et al. Removal of Hg⁰ from a simulated flue gas by photocatalytic oxidation on Fe and Ce co-doped TiO₂ under low temperature. *Chem Eng J* 2019, 360, 1530-1541.
- [17] Zhao SW, Zuo HF, Guo YR, et al. Carbon-doped ZnO aided by carboxymethyl cellulose: Fabrication, photoluminescence and photocatalytic applications. *J Alloys Compd* 2017, 695, 1029-1037.
- [18] Zhao W, Zhong Q, Pan YX, et al. Systematic effects of S-doping on the activity of V₂O₅/TiO₂ catalyst for low-temperature NH₃-SCR. *Chem Eng J* 2013, 228, 815-823.
- [19] Kayani ZN, Anjum M, Riaz S, et al. Role of Mn in biological, optical, and magnetic properties ZnO nano-particles. *Appl Phys A: Mater. Sci Process* 2020, 126, 197.
- [20] Ashebir ME, Tesfamariam GM, Nigussie GY, et al. Structural, optical, and photocatalytic activities of

- Ag-doped and Mn-doped ZnO nanoparticles. *J Nanomater* 2018, 2018, 938-947.
- [21] Qiu YF, Fan HB, Tan GP, et al. Effect of nitrogen doping on the photo-catalytic properties of nitrogen doped ZnO tetrapods. *Mater Lett* 2014, 131, 64-66.
- [22] Ditta MA, Farrukh MA, Ali S, et al. X-ray peak profiling, optical parameters and catalytic properties of pure and CdS doped ZnO-NiO nanocomposites. *Russ J Appl Chem* 2017, 90, 151-159.
- [23] Etacheri V, Roshan R, Kumar V. Mg-doped ZnO nanoparticles for efficient sunlight-driven photocatalysis. *ACS Appl Mater Interfaces* 2012, 4, 2717-2725.
- [24] Han J, An HJ, Kim TW, et al. Effect of structure-controlled ruthenium oxide by nanocasting in electrocatalytic oxygen and chlorine evolution reactions in acidic conditions. *Catalysts* 2019, 9, 549.
- [25] Peng F, Zhou CM, Wang HJ, et al. The role of RuO₂ in the electrocatalytic oxidation of methanol for direct methanol fuel cell. *Catal Commun* 2009, 10, 533-537.
- [26] Yue H, Xue LZ, Chen F. Efficiently electrochemical removal of nitrite contamination with stable RuO₂-TiO₂/Ti electrodes. *Appl Catal B* 2017, 206, 683-691.
- [27] Dalal B, Sarkar B, De SK. Itinerant to localized electronic behavior in phase segregated ruthenates. *J Alloys Compd* 2016, 667, 248-254.
- [28] Mariolacos K. The Role of The role of electronegativity in solid solution formation: An addendum. *Neues Jahrb Mineral Monatsh* 2003, 5, 215-221.
- [29] Liu ZF, E L, Ya J, et al. Growth of ZnO nanorods by aqueous solution method with electrodeposited ZnO seed layers. *Appl Surf Sci* 2009, 255, 6415-6420.
- [30] Alam U, Khan A, Raza W, et al. Highly efficient Y and V co-doped ZnO photocatalyst with enhanced dye sensitized visible light photocatalytic activity. *Catal Today* 2017, 284, 169-178.
- [31] Gomez-Pozos H, Gonzalez-Vidal JL, Torres GA, et al. Castaneda, Chromium and ruthenium-doped zinc oxide thin films for propane sensing applications. *Sensors* 2013, 13, 3432-3444.
- [32] Khan MAM, Kumar S, Alhazaa AN, et al. Al-Gawati, Modifications in structural, morphological, optical and photocatalytic properties of ZnO:Mn nanoparticles by sol-gel protocol. *Mater Sci Semicond Process* 2018, 87, 134-141.
- [33] Son HS, Choi NJ, Kim KB, et al. Al-doped ZnO seed layer-dependent crystallographic control of ZnO nanorods by using electrochemical deposition. *Mater Res Bull* 2016, 82, 50-54.
- [34] Deraz NM. Effects of heat treatment on physicochemical properties of cerium based nickel system. *J Anal Appl Pyrolysis* 2012, 95, 56-60.
- [35] Deraz NM. Effect of NiO content on structural, surface and catalytic characteristics of nano-crystalline NiO/CeO₂ system. *Ceram Int* 2012, 38, 747-753.
- [36] Chan HYH, Takoudis CC, Weaver MJ. High-pressure oxidation of ruthenium as probed by surface-enhanced Raman and X-ray photoelectron spectroscopies. *J Catal* 1997, 172, 336-345.
- [37] Kleiman-Shwarscstein A, Laursen AB, Cavalca F, et al. A general route for RuO₂ deposition on metal oxides from RuO₄. *Chem Commun* 2012, 48, 967-969.
- [38] Wang FZ, Xu Q, Tan ZA, et al. Efficient polymer solar cells with a solution-processed and thermal annealing-free RuO₂ anode buffer layer. *J Mater Chem A* 2014, 2, 1318-1324.
- [39] Ananth A, Dharaneedharan S, Gandhi MS, et al. Novel RuO₂ nanosheets-Facile synthesis, characterization and application. *Chem Eng J* 2013, 223, 729-736.
- [40] Cox PA, Goodenough JB, Tavener PJ, et al. The electronic structure of Bi_{2-x}Gd_xRu₂O₇ and RuO₂: A study by electron spectroscopy. *J Solid State Chem* 1986, 62, 360-370.
- [41] Kwak I, Kwon IS, Kim J, et al. IrO₂-ZnO hybrid nanoparticles as highly efficient trifunctional electrocatalysts. *J Phys Chem C* 2017, 121, 14899-14906.

- [42] Jing LQ, Xu ZL, Shang J, et al. The preparation and characterization of ZnO ultrafine particles. *Materials Science and Engineering a-Mater Sci Eng A* 2002, 332, 356-361.
- [43] Karamat S, Rawat RS, Tan TL, et al. Exciting dilute magnetic semiconductor: Copper-doped ZnO. *J Supercond Novel Magn* 2013, 26, 187-195.
- [44] Kostova B, Konstantinov L. Factors determining optical absorption of variously doped single crystals of $\text{Bi}_{12}\text{SiO}_{20}$. *J Phys Conf Ser* 2010, 253, 012029.
- [45] Bendavid LI, Carter EA, First principles study of bonding, adhesion, and electronic structure at the $\text{Cu}_2\text{O}(111)/\text{ZnO}(10\bar{1}0)$ interface. *Surf Sci* 2013, 618, 62-71.
- [46] Shao YQ, Chen ZJ, Zhu JQ, et al. Relationship between electronic structures and capacitive performance of the electrode material $\text{IrO}_2\text{-ZrO}_2$. *J Am Ceram Soc* 2016, 99, 2504-2511.
- [47] Gonzalez-Hernandez R, Perez WL, Rodriguez MJA. Electronic structure and magnetism in $\text{Ni}_{0.0625}\text{Zn}_{0.9375}\text{O}$: An ab initio study. *J Magn Magn Mater* 2009, 321, 2547-2549.
- [48] Wu HC, Peng YC, Chen CC. Effects of Ga concentration on electronic and optical properties of Ga-doped ZnO from first principles calculations. *Opt Mater* 2013, 35, 509-515.
- [49] Lakel S, Elhamra F, Almi K, et al. First-principles investigation of electronic and optical properties and thermodynamic stability of $\text{Zn}_{1-x}\text{Be}_x\text{O}$ semiconductor alloy. *Mater Sci Semicond Process* 2015, 40, 803-810.
- [50] Davis EA, Mott NF. Conduction in non-crystalline systems V. Conductivity, optical absorption and photoconductivity in amorphous semiconductors. *Philos Mag* 1970, 22, 0903-0922.
- [51] Liu HY, Zeng F, Lin YS, et al. Correlation of oxygen vacancy variations to band gap changes in epitaxial ZnO thin films. *Appl Phys Lett* 2013, 102, 181908.
- [52] Chen ZJ, Zhu JQ, Zhang S, et al. Influence of the electronic structures on the heterogeneous photoelectrocatalytic performance of $\text{Ti}/\text{Ru}_x\text{Sn}_{1-x}\text{O}_2$ electrodes. *J Hazard Mater* 2017, 333, 232-241.
- [53] Zhang X, Wang JM, Liu J, et al. Design and preparation of a ternary composite of graphene oxide/carbon dots/polypyrrole for supercapacitor application: Importance and unique role of carbon dots. *Carbon* 2017, 115, 134-146.
- [54] Shao YQ, Yi ZY, He C, et al. Effects of annealing temperature on the structure and capacitive performance of nanoscale $\text{Ti}/\text{IrO}_2\text{-ZrO}_2$ electrodes. *J Am Ceram Soc* 2015, 98, 1485-1492.
- [55] Vaiano V, Matarangolo M, Murcia JJ, et al. Enhanced photocatalytic removal of phenol from aqueous solutions using ZnO modified with Ag. *Appl Catal B* 2018, 225, 197-206.
- [56] Boudenne JL, Cerclier O, Galea J, et al. Electrochemical oxidation of aqueous phenol at a carbon black slurry electrode. *Appl. Catal., A* 1996, 143, 185-202.
- [57] Comminellis C. Electrocatalysis in the electrochemical conversion/combustion of organic pollutants for waste-water treatment. *Electrochim Acta* 1994, 39, 1857-1862.
- [58] Pelegrini R, Peralta-Zamora P, de Andrade AR, et al. Electrochemically assisted photocatalytic degradation of reactive dyes. *Appl Catal B* 1999, 22, 83-90.
- [59] Konstantinou IK, Albanis TA. TiO_2 -assisted photocatalytic degradation of azo dyes in aqueous solution: kinetic and mechanistic investigations - A review. *Appl Catal B* 2004, 49, 1-14.
- [60] Himebaugh R, Smith M. Semi-micro tube method for chemical oxygen demand. *Anal Chem* 1979, 51, 1085-1087.
- [61] Wei L, Zhu H, Mao XH, et al. Electrochemical oxidation process combined with UV photolysis for the mineralization of nitrophenol in saline wastewater. *Sep Purif Technol* 2011, 77, 18-25.

Figures

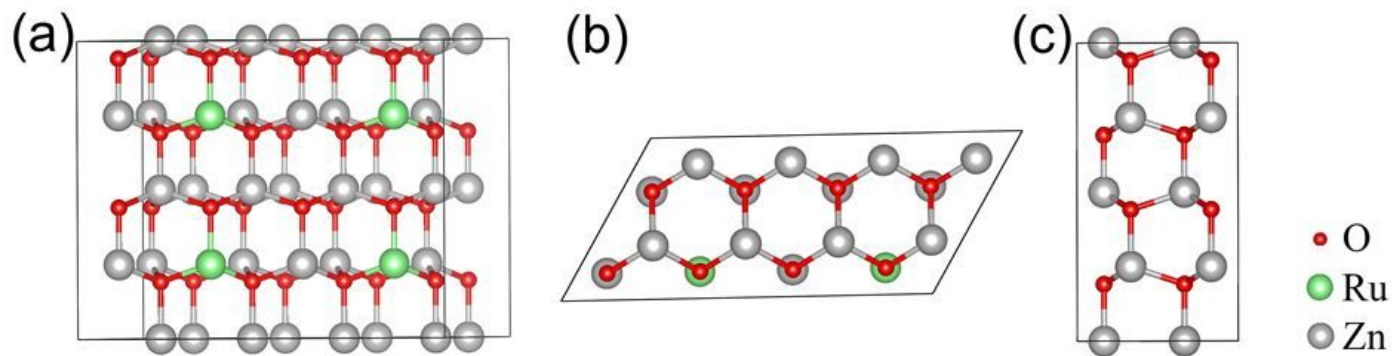


Figure 1

Ru-doped ZnO with hexagonal wurtzite crystal structure (a) front view; (b) top view; (c) left view. 2.4 Electrochemical measurements

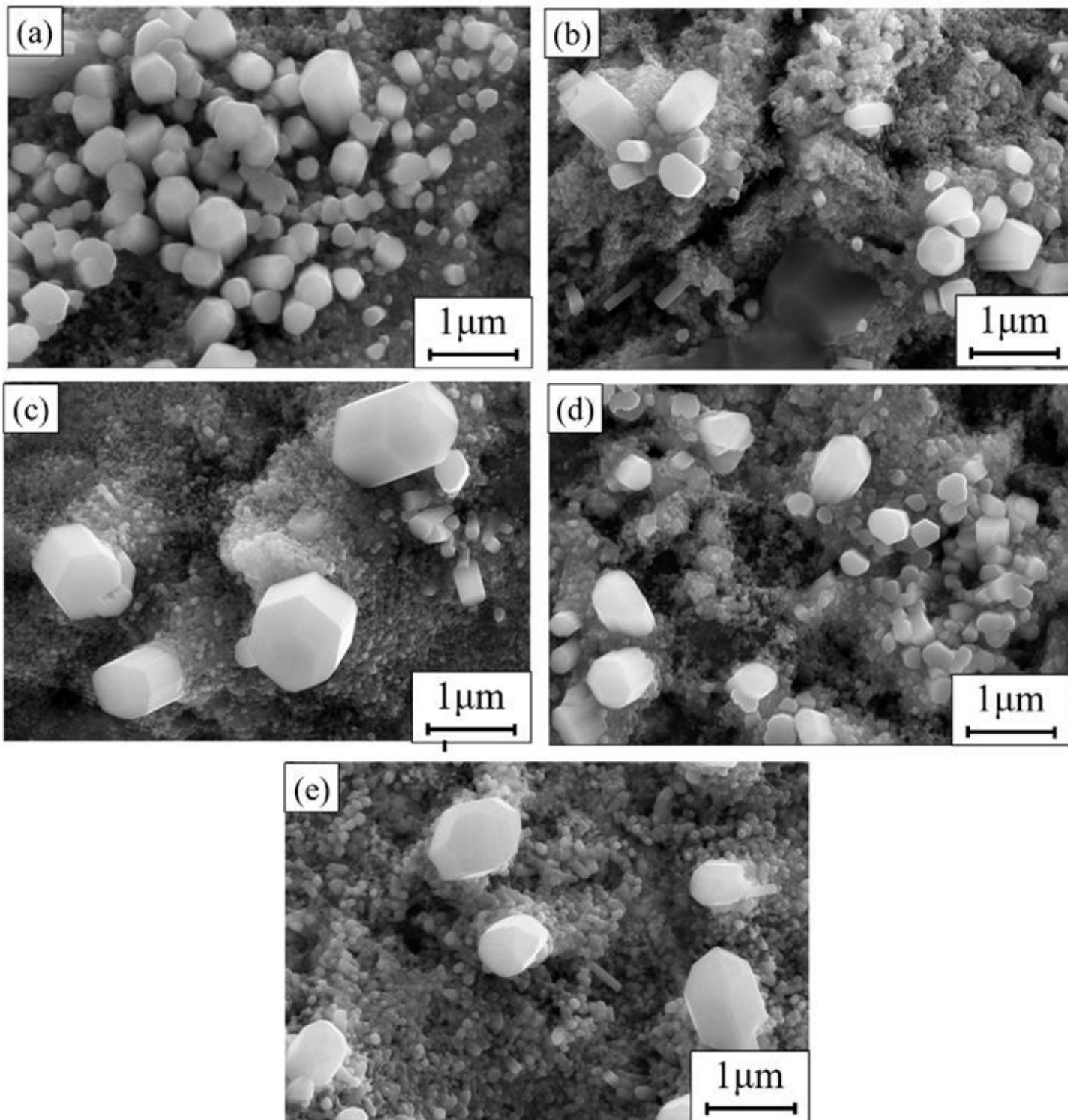


Figure 2

SEM images of $Ru_xZn_{1-x}O/Ti$ electrodes (a) 0mol%; (b) 3.125mol%; (c) 6.25mol%; (d) 9.375mol%; (e) 12.5mol%.

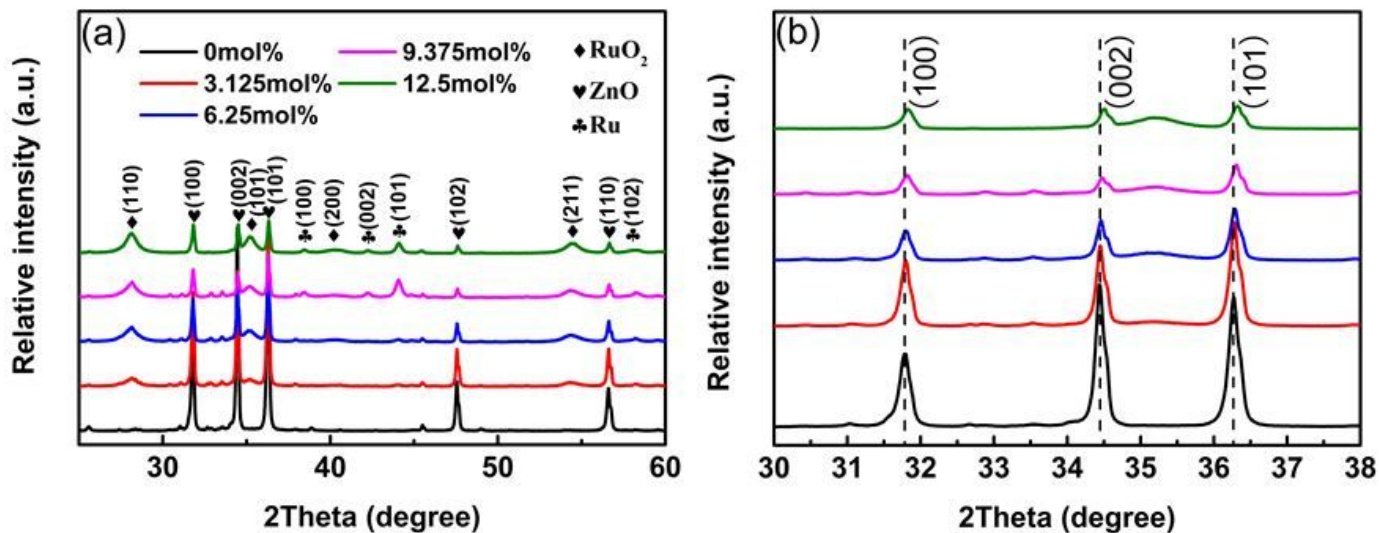


Figure 3

XRD patterns of Ru_xZn_{1-x}O/Ti electrodes (a) 2θ within 25-60°; (b) enlarged view of 2θ within 30-38°.

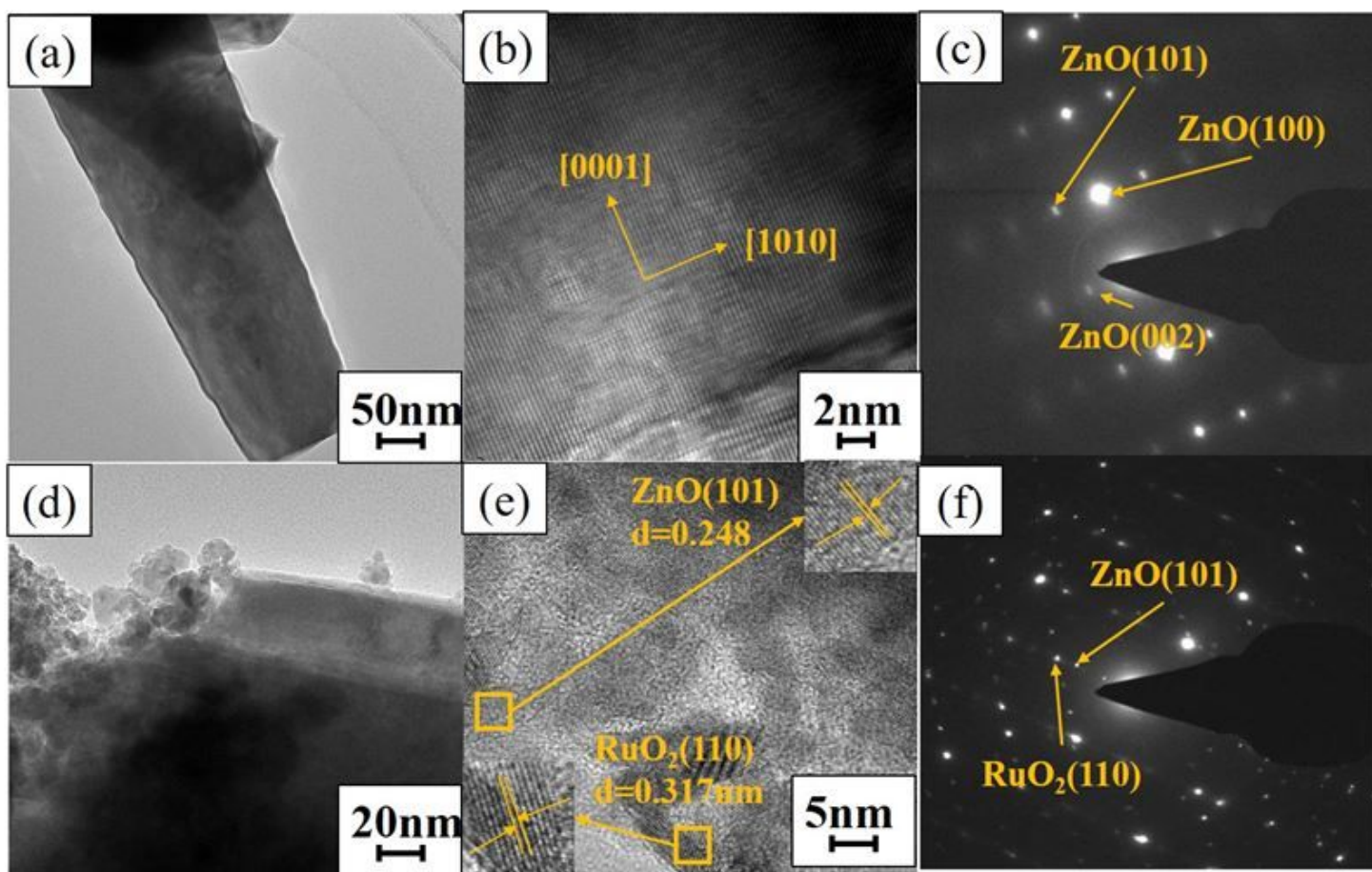


Figure 4

TEM and SAED patterns of Ru_xZn_{1-x}O/Ti electrodes (a, b, c) 0 mol%; (d, e, f) 9.375 mol%.

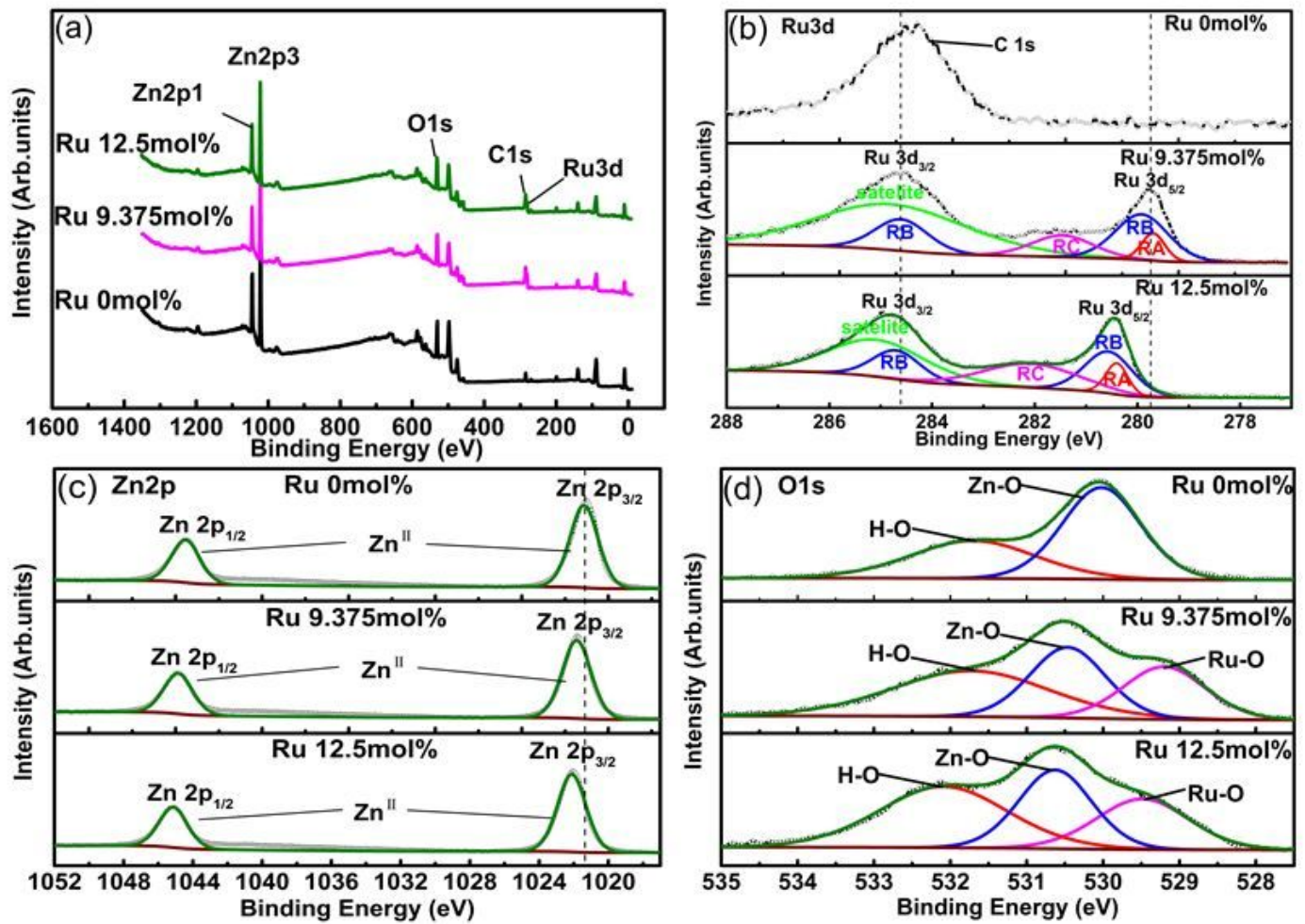


Figure 5

XPS spectra of Ru_xZn_{1-x}O/Ti coatings (a) full spectra; (b) Ru 3d; (c) Zn 2p; (d) O 1s.

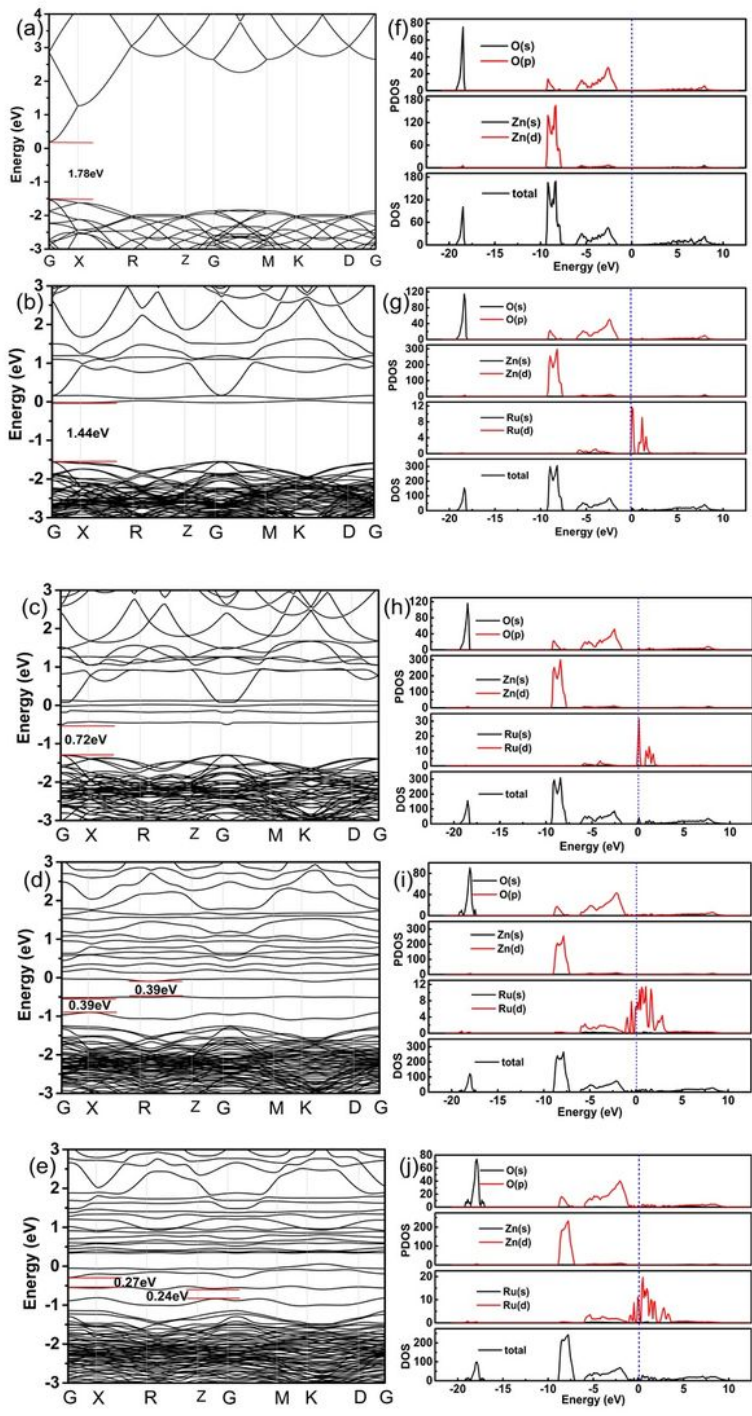


Figure 6

Band structure and density of state of the $\text{Ru}_x\text{Zn}_{1-x}\text{O}$ solid solution (a, f) 0mol%; (b, g) 3.125mol%; (c, h) 6.25mol%; (d, i) 9.375mol%; (e, j) 12.5mol%.

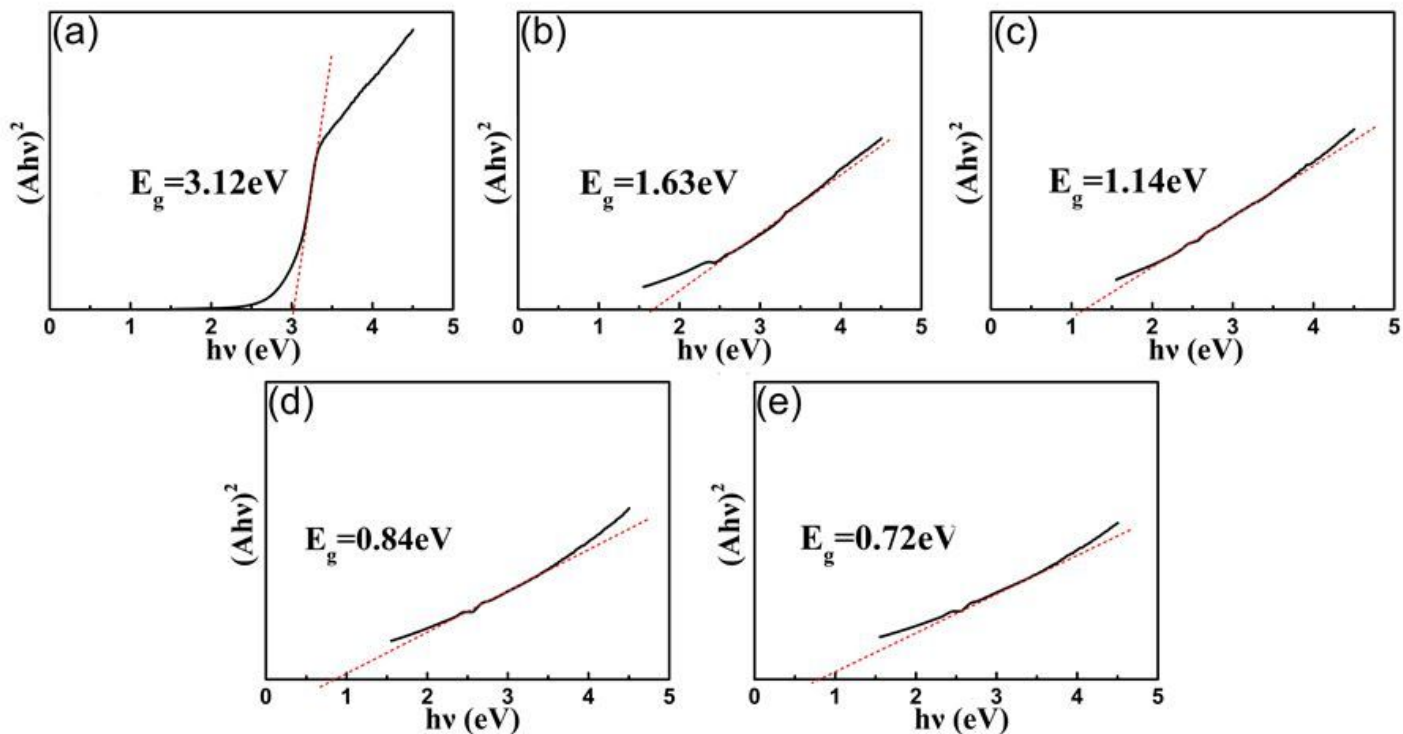


Figure 7

The UV-DRS patterns of the Ru_xZn_{1-x}O/Ti coatings (a) 0mol%; (b) 3.125mol%; (c) 6.25mol%; (d) 9.375mol%; (e) 12.5mol%.

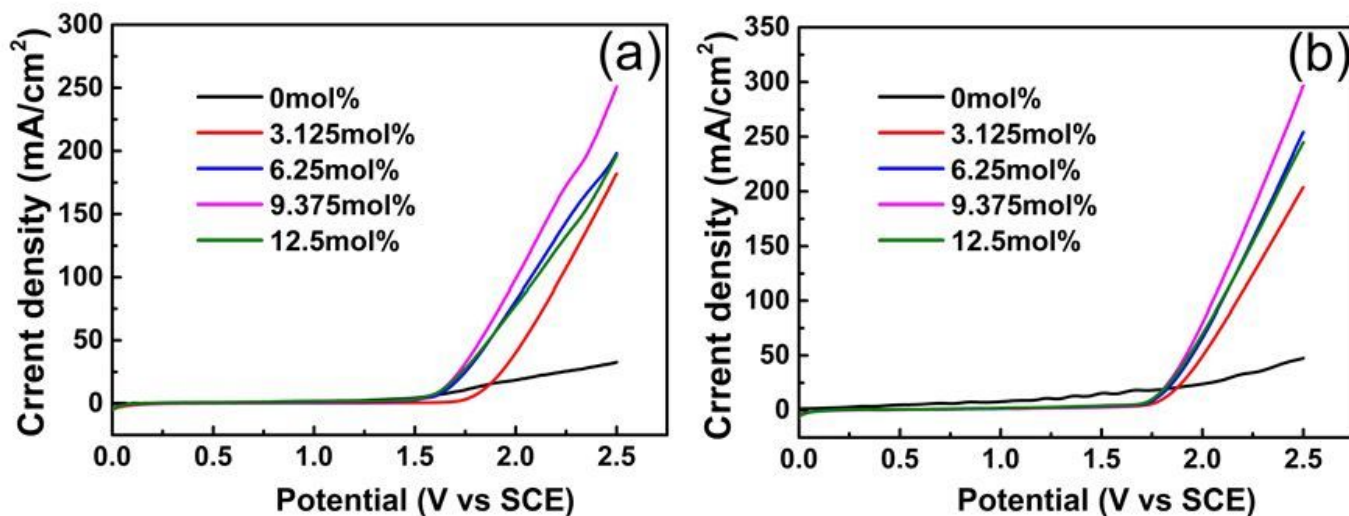


Figure 8

The LSV curves of the Ru_xZn_{1-x}O/Ti electrodes (a) without UV irradiation; (b) with UV irradiation.

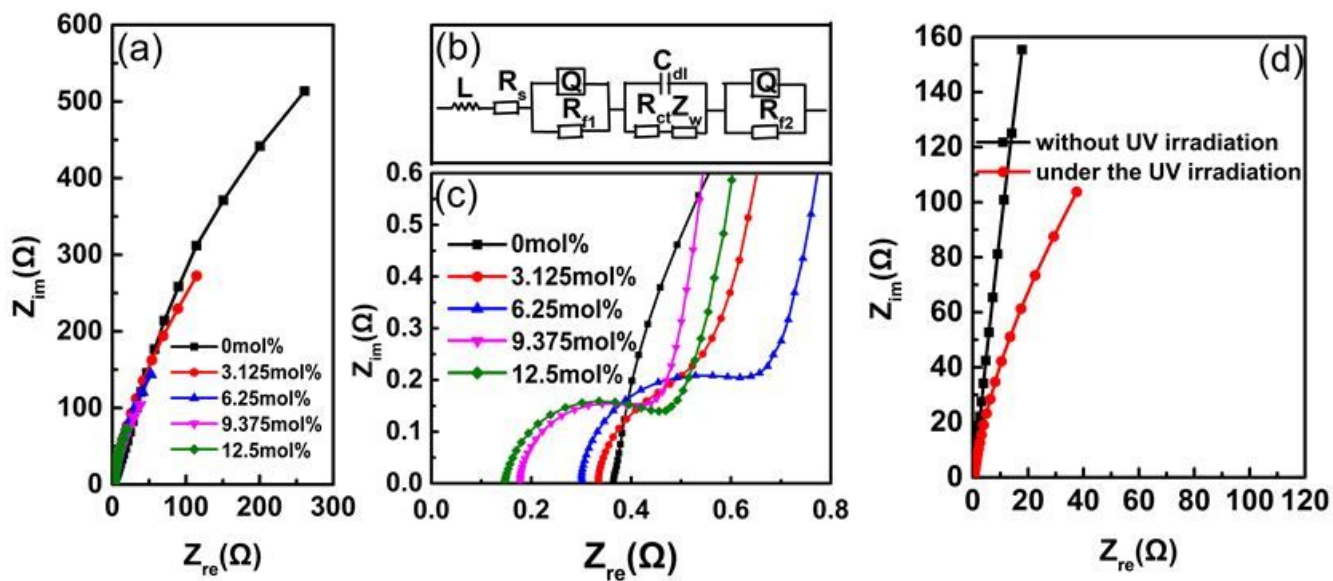


Figure 9

(a) Nyquist plots of the $Ru_xZn_{1-x}O/Ti$ electrodes; (b) the electrical equivalent circuit for the fitting of the impedance spectra; (c) the enlarged view of the high frequency region of the Nyquist plots; (d) the Nyquist plots with and without UV irradiation.

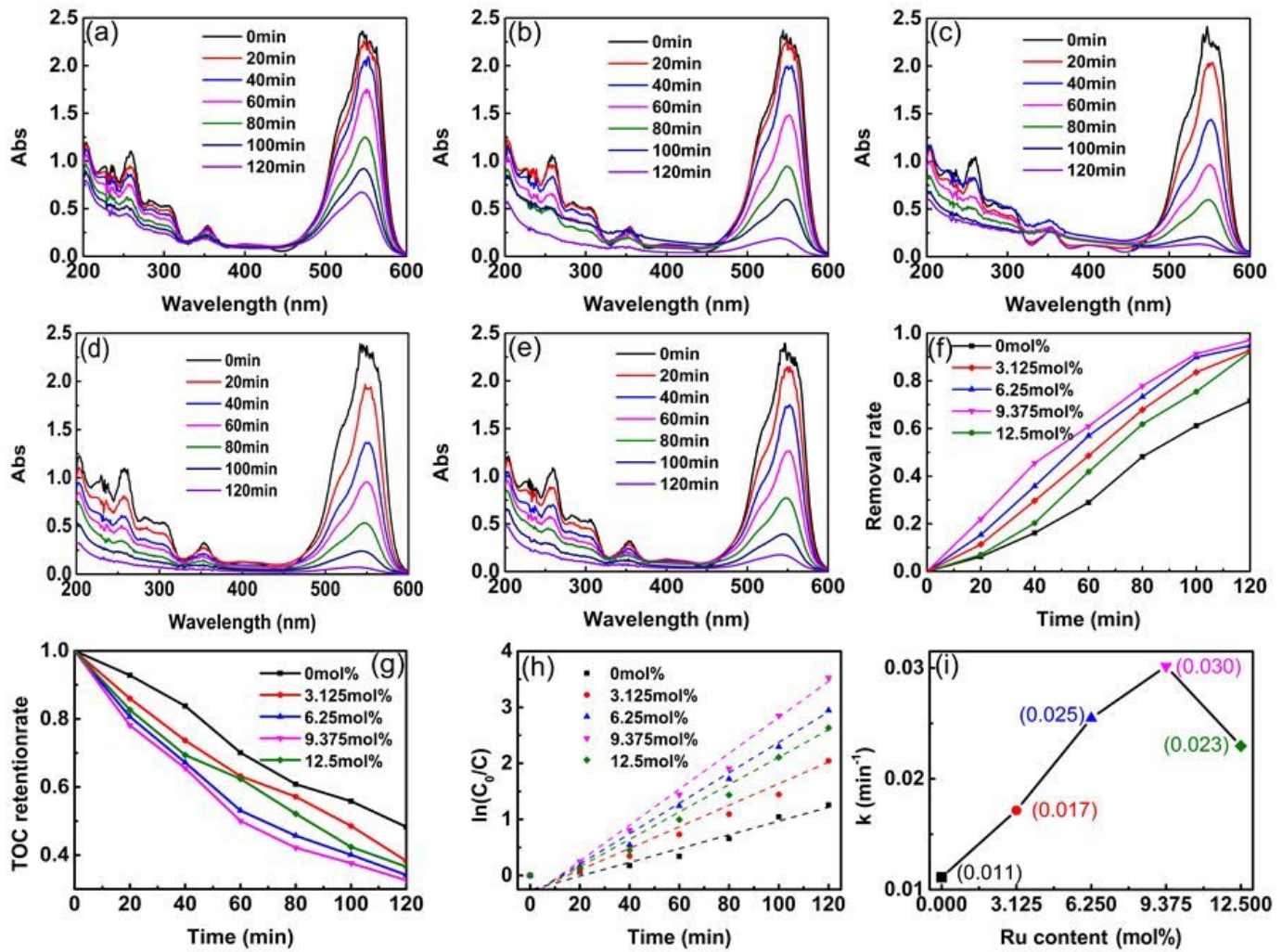


Figure 10

UV-vis absorption spectra of Ru_xZn_{1-x}O/Ti electrodes under PEC degradation with different intervals (a) 0 mol%; (b) 3.125 mol%; (c) 6.25 mol%; (d) 9.375 mol%; (e) 12.5 mol%; along with (f) removal ratio of RhB; (g) removal ratio of TOC; (h) degradation kinetics; (i) the reaction rate constant.

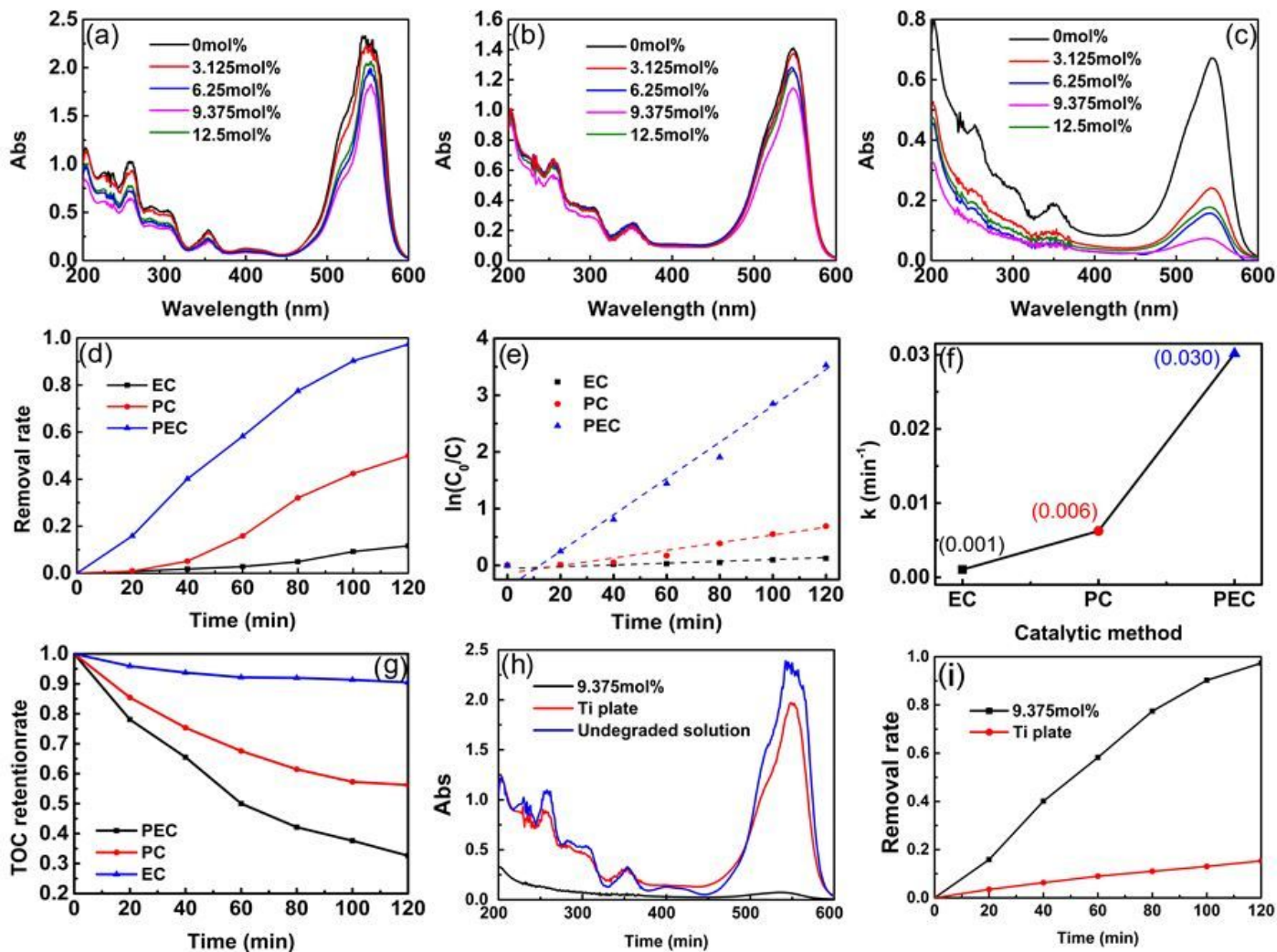


Figure 11

UV-visible absorption spectra of Ru_xZn_{1-x}O/Ti electrodes containing of 9.375mol% Ru with different catalytic methods (a) EC; (b) PC; (c) PEC; (d) removal rates of PEC, PC and EC; (e) degradation kinetics; (f) reaction rate constant; (g) TOC removal rates of PEC, PC and EC; (h) Comparison UV-visible absorption spectra after 120 min degradation; (i) removal rates of electrodes containing 9.375mol% Ru and Ti plates.

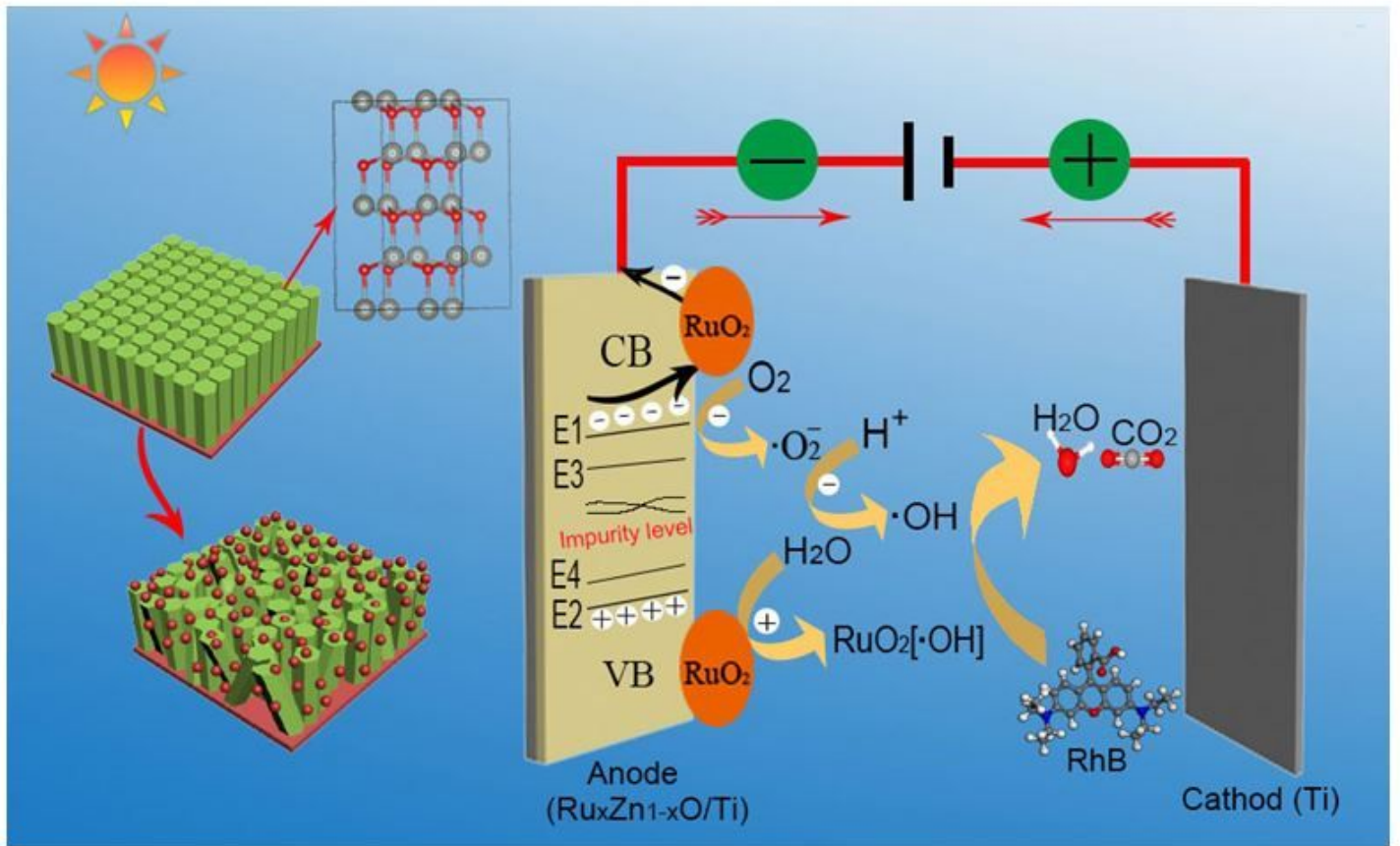


Figure 12

Schematic microstructure model and PEC mechanism of $\text{Ru}_x\text{Zn}_{1-x}\text{O}/\text{Ti}$ electrodes.